

EUROPEAN ORGANISATION FOR NUCLEAR RESEARCH (CERN)



October 4, 2019

Report from the NA61/SHINE experiment at the CERN SPS

The NA61/SHINE Collaboration

This document reports on the status and plans of the NA61/SHINE experiment at the CERN SPS as of October 2019. The document refers to the proposal SPSC-P-330.

Contents

1	Introduction	5
2	Data-taking summary	5
3	Software and calibration modifications	6
3.1	Native <u>SHINE</u> Software	6
3.2	Calibration	7
4	New results	9
4.1	New results for strong interactions physics	9
4.2	New results for neutrino physics	26
4.3	New results for cosmic-ray physics	29
5	Detector upgrade	37
5.1	TPC Upgrade	37
5.2	TDAQ Upgrade	42
5.3	VD Upgrade	45
5.4	DCS Upgrade	48
5.5	PSD Upgrade	49
5.6	MRPC Upgrade	51
5.7	Software Upgrade	55
5.8	Upgrade funding and spending profiles	56
6	Summary	58

The NA61/SHINE Collaboration

A. Aduszkiewicz¹⁵, E.V. Andronov²¹, T. Antičić³, V. Babkin¹⁹, M. Baszczyk¹³, S. Bhosale¹⁰, A. Blondel²³, M. Bogomilov², A. Brandin²⁰, A. Bravar²³, W. Bryliński¹⁷, J. Brzychczyk¹², M. Buryakov¹⁹, O. Busygina¹⁸, A. Bzdak¹³, H. Cherif⁶, M. Ćirković²², M. Csanad⁷, J. Cybowska¹⁷, T. Czopowicz¹⁷, A. Damyanova²³, N. Davis¹⁰, M. Deliyergiyev⁹, M. Deveaux⁶, A. Dmitriev¹⁹, W. Dominik¹⁵, P. Dorosz¹³, J. Dumarchez⁴, R. Engel⁵, G.A. Feofilov²¹, L. Fields²⁴, Z. Fodor^{7,16}, A. Garibov¹, M. Gaździcki^{6,9}, O. Golosov²⁰, V. Golovatyuk¹⁹, M. Golubeva¹⁸, K. Grebieszko¹⁷, F. Guber¹⁸, A. Haesler²³, S.N. Igolkin²¹, S. Ilieva², A. Ivashkin¹⁸, S.R. Johnson²⁵, K. Kadija³, E. Kaptur¹⁴, N. Kargin²⁰, E. Kashirin²⁰, M. Kiełbowicz¹⁰, V.A. Kireyeu¹⁹, V. Klochko⁶, V.I. Kolesnikov¹⁹, D. Kolev², A. Korzenev²³, V.N. Kovalenko²¹, K. Kowalik¹¹, S. Kowalski¹⁴, M. Koziel⁶, A. Krasnoperov¹⁹, W. Kucewicz¹³, M. Kuich¹⁵, A. Kurepin¹⁸, D. Larsen¹², A. László⁷, T.V. Lazareva²¹, M. Lewicki¹⁶, K. Łojek¹², B. Łysakowski¹⁴, V.V. Lyubushkin¹⁹, M. Maćkowiak-Pawłowska¹⁷, Z. Majka¹², B. Maksiak¹¹, A.I. Malakhov¹⁹, D. Manić²², A. Marcinek¹⁰, A.D. Marino²⁵, K. Marton⁷, H.-J. Mathes⁵, T. Matulewicz¹⁵, V. Matveev¹⁹, G.L. Melkumov¹⁹, A.O. Merzlaya¹², B. Messerly²⁶, Ł. Mik¹³, S. Morozov^{18,20}, S. Mrówczyński⁹, Y. Nagai²⁵, M. Naskręt¹⁶, V. Ozvenchuk¹⁰, V. Paolone²⁶, O. Petukhov¹⁸, R. Płaneta¹², P. Podlaski¹⁵, B.A. Popov^{19,4}, B. Porfy⁷, M. Posiadała-Zezula¹⁵, D.S. Prokhorova²¹, D. Pszczel¹¹, S. Puławski¹⁴, J. Puzović²², M. Ravonel²³, R. Renfordt⁶, E. Richter-Wąs¹², D. Röhrich⁸, E. Rondio¹¹, M. Roth⁵, B.T. Rumberger²⁵, M. Rumyantsev¹⁹, A. Rustamov^{1,6}, M. Rybczynski⁹, A. Rybicki¹⁰, A. Sadovsky¹⁸, K. Schmidt¹⁴, I. Selyuzhenkov²⁰, A.Yu. Seryakov²¹, P. Seyboth⁹, M. Słodkowski¹⁷, P. Staszal¹², G. Stefanek⁹, J. Stepaniak¹¹, M. Strikhanov²⁰, H. Ströbele⁶, T. Šušar³, A. Taranenko²⁰, A. Tefelska¹⁷, D. Tefelski¹⁷, V. Tereshchenko¹⁹, A. Toia⁶, R. Tsenov², L. Turko¹⁶, R. Ulrich⁵, M. Unger⁵, F.F. Valiev²¹, D. Veberič⁵, V.V. Vechernin²¹, A. Wickremasinghe²⁶, Z. Włodarczyk⁹, A. Wojtaszek-Szwarc⁹, O. Wyszynski¹², E.D. Zimmerman²⁵, and R. Zwaska²⁴

¹ National Nuclear Research Center, Baku, Azerbaijan

² Faculty of Physics, University of Sofia, Sofia, Bulgaria

³ Ruđer Bošković Institute, Zagreb, Croatia

⁴ LPNHE, University of Paris VI and VII, Paris, France

⁵ Karlsruhe Institute of Technology, Karlsruhe, Germany

⁶ University of Frankfurt, Frankfurt, Germany

⁷ Wigner Research Centre for Physics of the Hungarian Academy of Sciences, Budapest, Hungary

⁸ University of Bergen, Bergen, Norway

⁹ Jan Kochanowski University in Kielce, Poland

¹⁰ Institute of Nuclear Physics, Polish Academy of Sciences, Cracow, Poland

¹¹ National Centre for Nuclear Research, Warsaw, Poland

¹² Jagiellonian University, Cracow, Poland

¹³ AGH - University of Science and Technology, Cracow, Poland

¹⁴ University of Silesia, Katowice, Poland

¹⁵ University of Warsaw, Warsaw, Poland

¹⁶ University of Wrocław, Wrocław, Poland

¹⁷ Warsaw University of Technology, Warsaw, Poland

¹⁸ Institute for Nuclear Research, Moscow, Russia

¹⁹ Joint Institute for Nuclear Research, Dubna, Russia

²⁰ National Research Nuclear University (Moscow Engineering Physics Institute), Moscow, Russia

²¹ St. Petersburg State University, St. Petersburg, Russia

²² University of Belgrade, Belgrade, Serbia

²³ University of Geneva, Geneva, Switzerland

²⁴ Fermilab, Batavia, USA

²⁵ University of Colorado, Boulder, USA

²⁶ University of Pittsburgh, Pittsburgh, USA

The NA61/SHINE Limited Members

N. Antoniou¹, P. Banasiak⁷, N. Benekos⁸, S. Bordini⁸, N. Charitonidis⁸, P. Christakoglou¹, A. Datta³, A. De Roeck⁸, F. Diakonos¹, P. von Doetinchem³, D. Gawliński⁷, M. Grzelak⁷, T. Hasegawa², S. Jędrzejewski⁷, A. Kapoyannis¹, J. Kempa⁷, T. Kobayashi², U. Kose⁸, D.R. Kowcun⁷, O. Linnyk⁵, B. Luis⁴, B. Meller⁷, S.A. Monsalve⁸, T. Nakadaira², K. Nishikawa², A.D. Panagiotou¹, T. Pawlak⁷, D. Piotrowski⁷, W. Rauch⁶, K. Sakashita², P. Sala⁸, S. Schramm⁵, T. Sekiguchi², D. Sgalaberna⁸, M. Shibata², A. Shukla³, J. Steinheimer-Froschauer⁵, M. Tada², M. Vassiliou¹, L. Whitehead⁸, J. Wiktorowicz⁷, and K. Zhou⁵

¹ University of Athens, Athens, Greece

² Institute for Particle and Nuclear Studies,
Tsukuba, Japan

³ University of Hawaii at Manoa, USA

⁴ Los Alamos National Laboratory, USA

⁵ Frankfurt Institute for Advanced Studies,

Frankfurt, Germany

⁶ Fachhochschule Frankfurt, Frankfurt, Germany

⁷ Warsaw University of Technology Plock Campus,
Poland

⁸ CERN, Geneva, Switzerland

1 Introduction

This NA61/SHINE annual report presents briefly the status and plans of the NA61/SHINE experiment [1] at the CERN SPS. The report refers to the period October 2018 – October 2019.

The document is organized as follows. The data taking summary is given in Section 2. Software and calibration modifications are listed in Sec. 3. New results are briefly reviewed in Sec. 4. Detector upgrade status and plans are presented in Sec. 5. The summary in Sec. 6 closes the report.

In 2018 NA61/SHINE provided input to prepare the discussions on the update of European Strategy for Particle Physics [2]. The NA61/SHINE input is included in the following documents:

- (i) Input to the European Particle Physics Strategy Update [3],
- (ii) Summary Report of Physics Beyond Colliders at CERN [4],
- (iii) Physics Beyond Colliders: QCD Working Group Report [5],
- (iv) Conclusions of the Neutrino Town Meeting [6],
- (v) Conclusions of the Heavy Ion Town Meeting [7].

2 Data-taking summary

As described in the 2017 status report, data taking with a replica of the NOvA target in summer 2018 suffered from problems with the cryogenics of the VERTEX-1 magnet, beam downtime and setup of the new DRS4 readout. Because of this statistics recorded in summer were below the goal, so in November 2018 NA61/SHINE continued data taking with the replica of the NovA target for one week. Additional 3.1 million p+NOvA replica target events at beam momentum of 120 GeV/c were collected.

Next, the experiment recorded 3.8 million Pb+Pb events at 150A GeV/c, with the Vertex Detector turned on, for measurements of open charm production, and for the study of collective effects and fluctuations.

At the end of this period 0.2 million events with the high intensity Pb beam at 150A GeV/c were taken to study the detector response in conditions expected after Long Shutdown 2. Finally a short run with defocused Pb beam was devoted to collect calibration data for the MOEDAL experiment at the LHC.

In the last week of the 2018 data taking period, the SPS delivered a secondary ion beam for a pilot run to study the feasibility of measuring nuclear fragmentation needed for cosmic-ray research with NA61/SHINE, see Sec. 4.3. 1.1 million ^{12}C beam triggers were recorded for physics analysis at a beam rigidity of $R = 27\text{ GV}$ alternating between a ^{12}C and polyethylene target.

In 2019 no data were taken due to the start of Long Shutdown 2. Instead, activities of the collaboration concentrated on the detector upgrade programme for post-LS2 running (see Sec. 5) in parallel to the physics analysis of data collected before 2019.

3 Software and calibration modifications

3.1 Native SHINE Software

3.1.1 SHINE framework

Since the previous report, five software releases were made. The most significant changes were:

- (i) migration to CentOS7 with SHINE dependencies provided via custom (SHINE still relies on ROOT v5) LCG views
- (ii) moving releases to CVMFS
- (iii) further development of the native reconstruction (see Sec. 1)
- (iv) implementation of Ar+Sc and Pb+Pb Monte Carlo configurations and scripts

In the course of the first 2 points all AFS ties were removed, so that all the software is provided via CVMFS, according to CERN IT policies. Also the release process was automated using a single Jenkins job to build sources in various configurations along with the doxygen documentation; the job signals completion to a cron task at the CVMFS publish machine which then automatically publishes new releases to CVMFS.

Introduction of LCG views to SHINE was associated with establishing permanent contact with the EP-SFT group and lead to a vivid and fruitful cooperation. The system for building LCG software, `lcgmake`, was incorporated in the NA61/SHINE workflow providing automation, documentation, reuse and compatibility with centrally maintained LCG software for building SHINE dependencies. The compatibility with centrally maintained LCG software will assure smoother transitions to new operating systems, compilers and package versions.

3.1.2 Monte Carlo simulation

Since the last Status Report 2018, no major change of the GEANT4-based Monte Carlo simulation chain in SHINE has been implemented. The latest SHINE Monte Carlo version is being used for physics analyses from low-multiplicity interactions (e.g. neutrino program utilizing hadron beams on light nuclear targets) to high-multiplicity interactions (e.g. Ar+Sc and Pb+Pb collisions). A fast PSD simulator is under development to avoid time and resource consuming GEANT4 simulation for mass production of high multiplicity heavy ion samples. Progress on the event reconstruction is discussed in the next section.

3.1.3 Event reconstruction

Development of the SHINE native reconstruction software is almost complete except for the development of the ToF module, see Fig. 1 for detail.

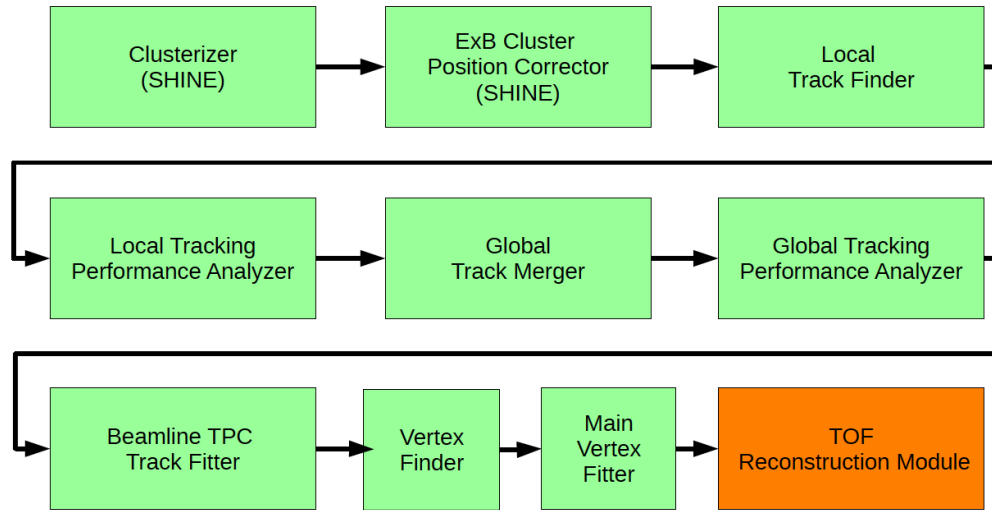


Figure 1: Status of the native SHINE event reconstruction software. Green boxes indicate ready-to-use modules and the orange box indicates the ToF module under development.

In addition to the existing main vertex reconstruction algorithms for thin and liquid hydrogen targets, a third vertex reconstruction algorithm for the neutrino replica long targets (T2K, NOvA) is under development.

3.2 Calibration

Data calibration activities and calibration software upgrades during last year included:

- (i) The reconstruction of events by "legacy" software was stopped as all data collected before 2016 and required for physics analysis was successfully calibrated.
- (ii) The reconstruction of NA61/SHINE data is now entirely processed using the HTCondor system.
- (iii) Data collected for the beam momentum of 13A GeV/c were fully reconstructed after recalibration of the magnetic field.
- (iv) A new manager for residual corrections of cluster positions was prepared and intensively used. The new manager is fully configurable by xmls files and the correction factors are now stored in a dedicated DB directory.
- (v) The neutrino data, especially p+C collisions at 120 GeV/c and π +Be, π +C collisions at 60 GeV/c, were almost fully calibrated (except for dE/dx calibration), validated and partly analysed.

- (vi) The calibration of Pb+Pb data samples collected at 13A and 30A GeV/c beam momentum was improved thanks to an additional TPC drift velocity adjustment and application of new TPC cluster position residual correction factors.
- (vii) The data from Xe+La collisions at 150A GeV/c beam momentum is partly calibrated. The TPC parameters like: time off-sets, drift velocities as a function of time and positions were obtained. The standard algorithm required modification because of the lack of measurements from the ToF detectors for a part of the events.
- (viii) The energy loss (dE/dx) calibration is ongoing using the "legacy" software. There is a significant progress in the conversion of this software to the SHINE framework. The SHINE software includes a new Bethe Bloch fitter.

3.2.1 A.I.-controlled TPC monitoring using physics data

Dedicated studies were performed aimed at providing precise quality control of the TPC electronics response. Unlike for the electronic pulser which gives only general information on the electronics status, or the krypton calibration procedure [8] which diagnoses the chamber in conditions resembling those of real physics data but only in large time intervals (several months or more), the present approach aims at providing an in-depth diagnosis of all the possible deteriorations of the TPC response for every NA61/SHINE dataset.

In the first steps of this effort, charge spectra obtained as a result of the radiative ^{83}Kr decay in the TPC ($\sim 200,000$ spectra for all the TPC channels) were classified using a Multi-layer Perceptron (MLP) supervised learning algorithm (python scikit-learn, `sklearn.neural_network.MLPClassifier` being a major component of the dedicated "neuralKr" module). The latter was trained using a sample of human eye-scans of the order of $\sim 5,000$ histograms per TPC, where each spectrum was pre-classified as either "good" or "bad" by eye inspection.

Subsequently, the latter algorithm was adapted to handle charge deposit spectra obtained from physics data (i.e., from tracks of charged particles produced in Ar+Sc collisions at 150A GeV/c beam momentum). A modified version of the original neural network (MLP) ("neuralArSc" module) was trained using the information on electronics channel quality provided by ^{83}Kr charge spectra eye-scans, attached however to the charge deposit spectra of Ar+Sc physics data of the corresponding channel. This method appeared more reliable than direct human eye-scans of dE/dx ionization spectra. The consistency of the two algorithms was investigated in detail and the response of the neuralArSc algorithm to changes that occurred in the time interval between Kr and Ar+Sc data taking was judged very satisfactory. It appeared in fact that the hybrid supervised learning algorithm (Ar+Sc data taken together with Kr labels) improved the selection criteria devised to localize TPC channels of inferior or deteriorated quality, and lowered the error margin induced by human eye-scans applied in the precedent neural network. The resulting quality map of the MTPC-L chamber electronics obtained directly from Ar+Sc collision data is presented in Fig. 2. As visible in the figure, no indication of serious deterioration was found. The improved neural network is planned to be applied for the high statistics Pb+Pb data taking after LS2.

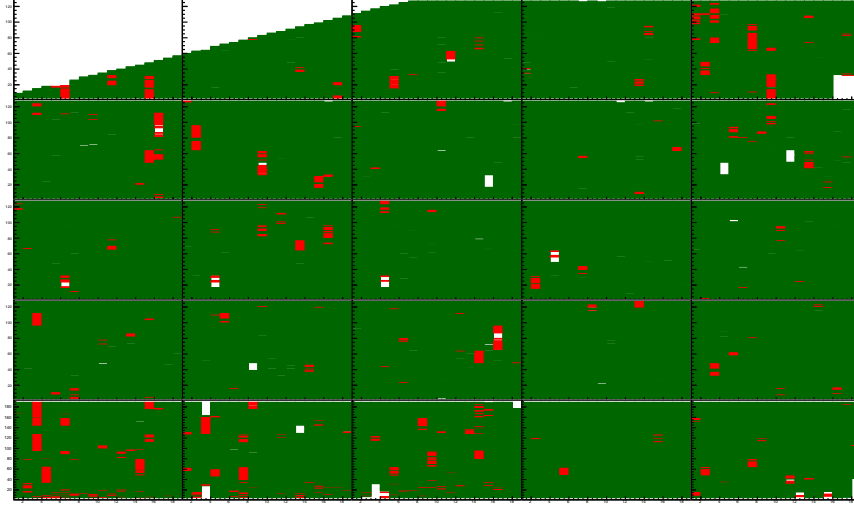


Figure 2: Quality map of MTPCL electronics obtained by the neural network from physics data on Ar+Sc collisions: channels with good (green), deteriorated (red) and no (white) signal are indicated.

4 New results

4.1 New results for strong interactions physics

This section summarizes new physics results from the programme on physics of strong interactions. The most recent results on spectra and yields as well as on fluctuations and correlations are presented. They are ordered and labelled according to the NA61/SHINE physics goals, i.e. the study of the onsets of deconfinement (OD) and fireball (OF), the search for the critical point (CP) and others (O).

4.1.1 (OD, OF) K^\pm spectra and yields in the 10% most central Ar+Sc collisions at 19A–150A GeV/c

Preliminary results on charged kaons from the the 10% most central Ar+Sc interactions were obtained and presented in Refs. [9, 10]. Both identification methods, namely dE/dx (analysis using TPC energy loss information to identify particles) and $tof-dE/dx$ (analysis determining the number of π , K , p using energy loss and particle time of flight measurements) were used to obtain double differential (y, p_T) spectra of charged kaons [9]. Results refer to primary particles produced in strong and electromagnetic processes and are corrected for geometrical detector acceptance and reconstruction efficiency as well as contamination from weak decays and secondary interactions. Only statistical uncertainties were obtained and studies of systematic uncertainties are in progress.

The mid-rapidity ($0 < y < 0.2$) transverse momentum spectra of K^\pm are presented in Fig. 3 for all analyzed energies. The points were fitted with the Boltzmann function and extrapolated beyond the detector acceptance. The function integral outside the acceptance

region was added to the measured data points allowing to obtain dn/dy spectra presented in Fig. 4.

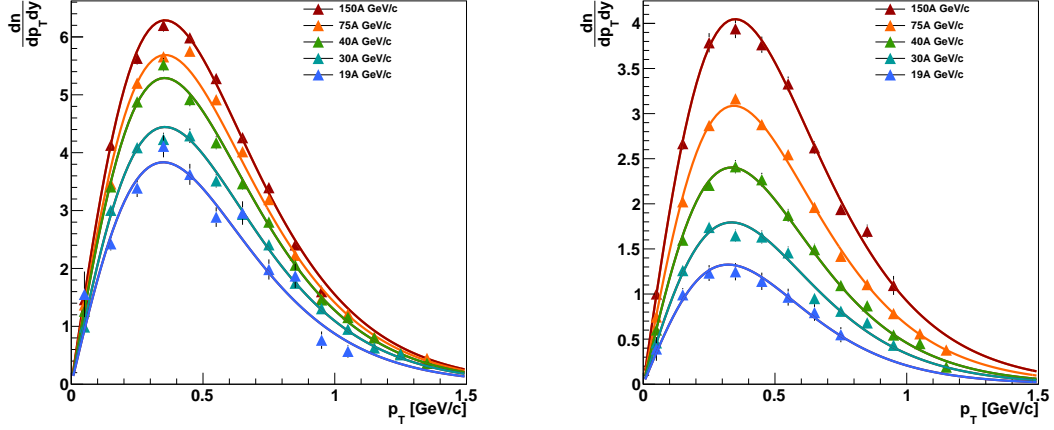


Figure 3: Preliminary results on mid-rapidity ($0 < y < 0.2$) transverse momentum spectra of K^+ (left) and K^- (right) mesons produced in the 10% most central Ar+Sc collisions at 19A–150A GeV/c. The lines correspond to the fitted Boltzmann functions. Only statistical uncertainties are shown.

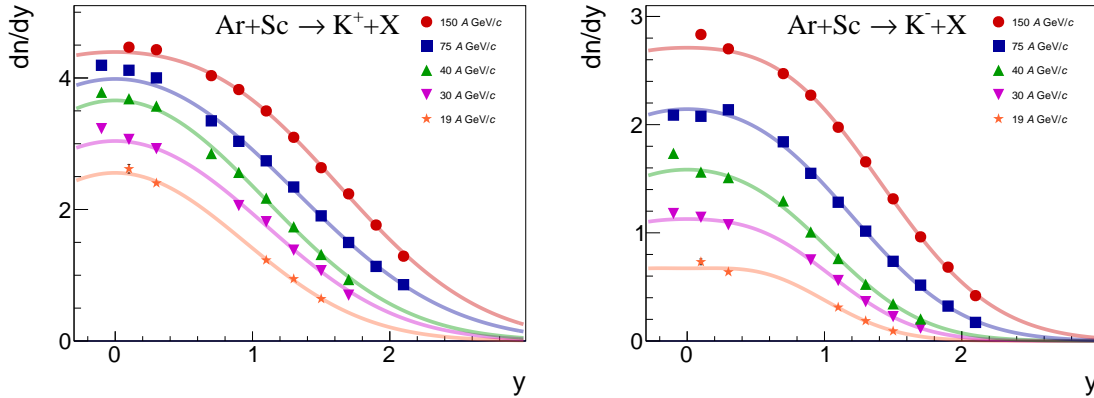


Figure 4: Preliminary results on rapidity spectra of K^+ (left) and K^- (right) mesons produced in the 10% most central Ar+Sc collisions at 19A–150A GeV/c. The lines correspond to the fitted sum of symmetrically displaced Gaussian functions. Only statistical uncertainties are shown.

Symmetry of the rapidity spectrum (Fig. 4) around $y = 0$ was assumed and the experimental points were fitted by a sum of two Gaussian functions symmetrically displaced around mid-rapidity to obtain the mean multiplicities of charged kaons.

Figures 5 and 6 show the current status of the *step* and *horn* plots. In Pb+Pb collisions a plateau in the dependence on $\sqrt{s_{NN}}$ of the inverse slope parameter of K^\pm spectra is observed. Such a structure was predicted due to mixed phase of hadron gas and QGP [11]. Figure 5 shows that similar structures are visible in other systems. However, the level of the plateau grows with the size of the collision system.

A rapid change (*horn*) was found in the energy dependence of K^+/π^+ and $\langle K^+ \rangle / \langle \pi^+ \rangle$ ratios for central Pb+Pb/Au+Au collisions, which is interpreted as due to the onset of de-

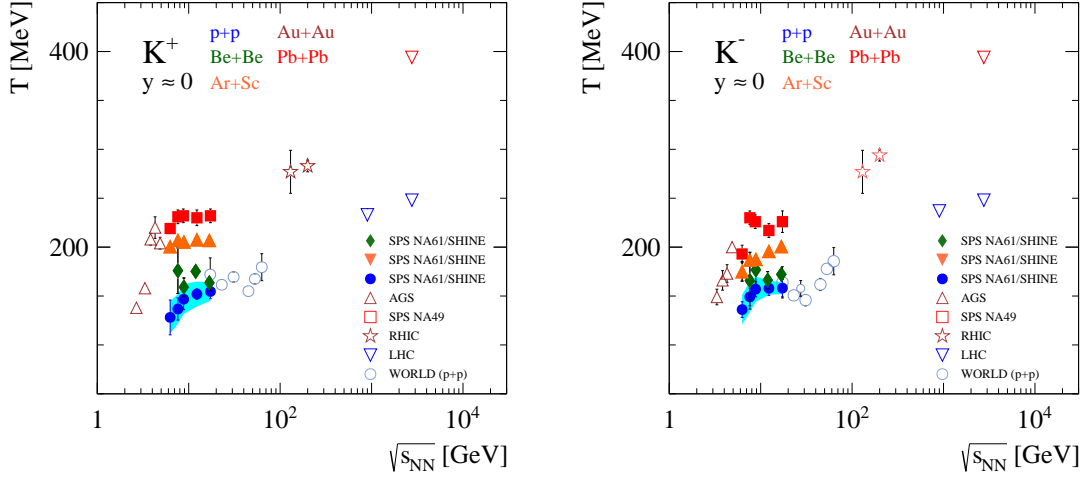


Figure 5: Inverse slope parameter of mid-rapidity transverse mass spectra of K^+ (left) and K^- (right) mesons as function of collision energy for p+p, Be+Be, Ar+Sc, and Pb+Pb/Au+Au collisions. NA61/SHINE results are preliminary.

confinement [11]. NA61/SHINE results show a plateau like structure in p+p interactions. Results from Be+Be collisions are close to those from p+p interactions. The new results on Ar+Sc interactions show dependence on collision energy qualitatively similar to p+p data, but the plateau is at a significantly higher level. Surprisingly, there is no indication of *horn* structure in the Ar+Sc data.

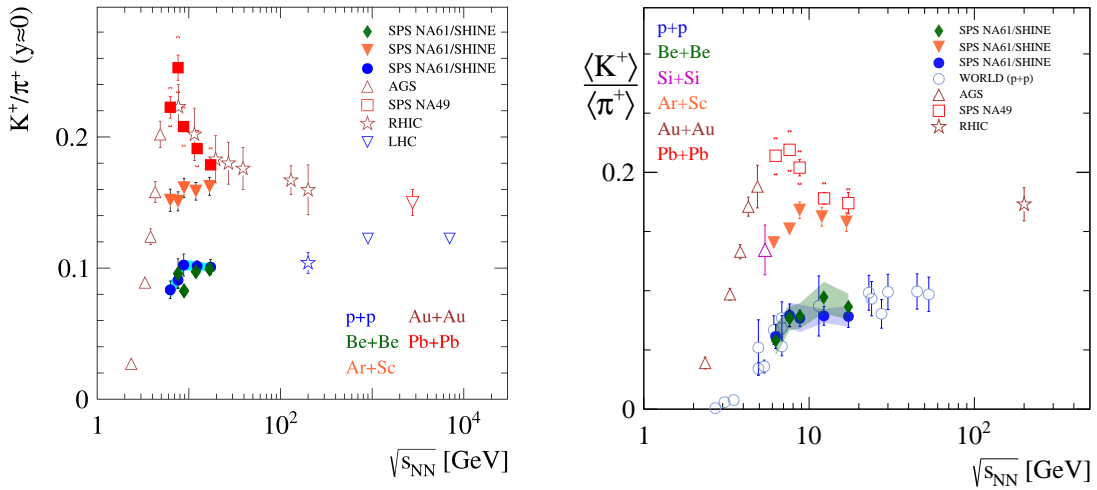


Figure 6: K^+/π^+ ratio at mid-rapidity (left) and $\langle K^+ \rangle / \langle \pi^+ \rangle$ ratio in full 4π phase space (right) as function of collision energy for p+p, Be+Be, Ar+Sc, and Pb+Pb/Au+Au collisions. NA61/SHINE Be+Be and Ar+Sc results are preliminary, p+p data are published in Ref. [12].

(OD, OF) Proton-proton interactions and onset of deconfinement

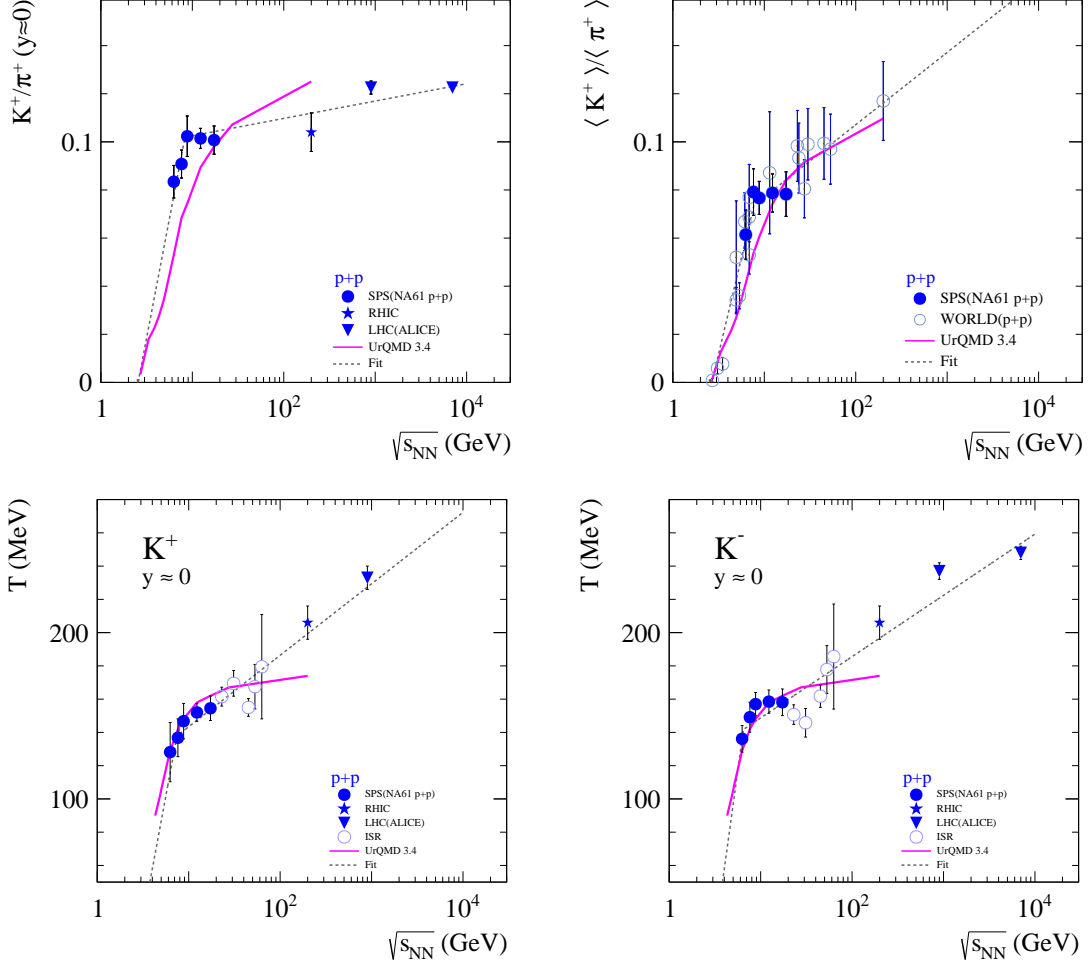


Figure 7: Top: K^+/π^+ ratio at mid-rapidity (left) and $\langle K^+ \rangle / \langle \pi^+ \rangle$ ratio in full 4π phase space (right) as function of collision energy for p+p data. Bottom: Inverse slope parameter of mid-rapidity transverse mass spectra of K^+ (left) and K^- (right) mesons as function of collision energy for p+p interactions.

The p+p results obtained by NA61/SHINE has been considered as a possible hint of the onset of deconfinement in small systems. Kaon to pion ratios, as well as the inverse slope parameter of m_T spectra are presented in Fig. 7 together with predictions of the UrQMD model predictions and results of the fits discussed below.

The collision energy dependence of the K^+/π^+ ratio in inelastic p+p interactions is different from the one in heavy-ion collisions (see Fig. 6). First of all, the ratio is smaller in p+p interactions than in Pb+Pb and Au+Au collisions and does not show the horn structure. Starting from the threshold energy the ratio in p+p interactions steeply increases to reach a plateau at CERN SPS energies. The plateau is followed by a weak increase towards LHC energies. Notably, the beginning of the plateau in p+p interactions coincides with the horn maximum in heavy-ion collisions.

The collision energy dependence of the T parameter in heavy-ion collisions shows the *step* structure (see Fig. 5). Following a fast rise the T parameter passes through a stationary region (or even a weak minimum for K^-), which starts at low SPS energies, and then (above the top SPS energy) enters a domain of steady increase. The increase continues up to the top LHC energy. The collision energy dependence of the T parameter in inelastic p+p interactions is surprisingly similar to the one for central Pb+Pb and Au+Au collisions. The main difference is that the T parameter in p+p interactions is significantly smaller than for heavy-ion collisions.

To estimate the break point between a fast rise at low energies and a plateau or slower increase at high energies two straight lines were fitted to the p+p data (Fig. 7). The low energy line was constrained by the threshold energy for kaon production. The fitted break energy is 8.3 ± 0.6 GeV, 7.70 ± 0.14 GeV, 6.5 ± 0.5 GeV and 7.9 ± 0.2 GeV, for the K^+/π^+ , $\langle K^+ \rangle / \langle \pi^+ \rangle$ ratios and $T(K^-)$, $T(K^+)$, respectively. These values are close to each other and surprisingly close to the energy of the beginning of the horn and step structures in central Pb+Pb collisions - the transition energy being approximately 8 GeV (see Figs. 5 and 6). Finally, the resonance-string model UrQMD fails to reproduce NA61/SHINE data (Fig. 7). A paper discussing these NA61/SHINE results was recently submitted to Nature Physics.

4.1.2 (OD) Anisotropic flow (v_1, v_2) of π^- and protons in Pb+Pb interactions at 13A GeV/c

The directed and elliptic flow relative to the projectile spectator plane were measured for Pb+Pb collisions at 13A GeV/c and shown in Ref. [13]. Results are presented for negatively charged pions and protons produced by strong interaction processes and their weak and electromagnetic decays (in the TPC acceptance [14]) and all hadrons at forward rapidity (in the PSD acceptance [15]). The results were corrected for detector azimuthal non-uniformity using the procedure described in Ref. [16]. No corrections for p_T and y tracking and particle identification (PID) efficiency were applied in the present analysis.

Figure 8 (left) shows results for negatively charged pion and proton v_1 as a function of p_T . The value of $v_1(p_T)$ approaches zero at zero p_T and for negatively charged pions changes

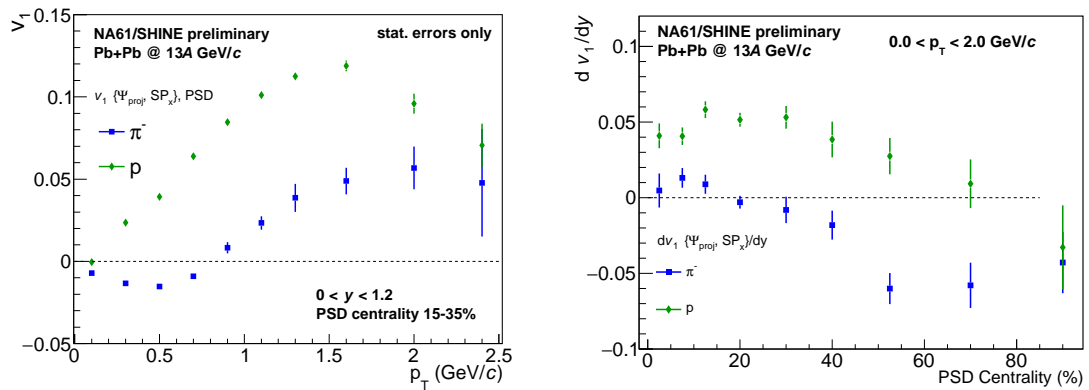


Figure 8: Left: negatively charged pion and proton directed flow $v_1(p_T)$ for the 15-35% centrality class. Right: slope of directed flow dv_1/dy at $y = y_{CM}$ as function of the collision centrality.

sign at $p_T \approx 0.7 - 1.3$ GeV/ c . The rate of change of directed flow, dv_1/dy , is shown in Fig. 8 (right) as function of collision centrality. It was calculated by fitting $v_1(y)$ for $|y| < 0.4$ with a linear function. For both protons and negative pions it starts with positive values for central collisions and turns to negative values for more peripheral collisions. This observation is consistent with recent STAR results from the RHIC Beam Energy Scan [17].

Directed and elliptic flow for Pb+Pb collisions at different energies are compared in Fig. 9. Directed flow (Fig. 9, left) shows strong collision energy dependence, in particular at the p_T where v_1 changes its sign.

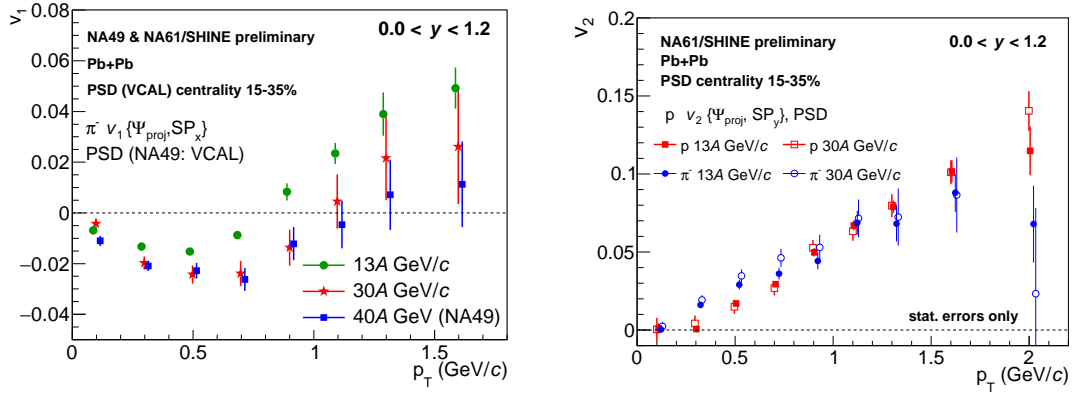


Figure 9: Left: negatively charged pion directed flow $v_1(p_T)$ for beam momenta 13A GeV/ c , 30A GeV/ c [18] and kinetic energy of 40A GeV [19]. Right: elliptic flow $v_2(p_T)$ for protons and negatively charged pions at beam momenta 13A and 30A GeV/ c .

Elliptic flow $v_2(p_T)$ differs for negative pions and protons (Fig. 9, right) and shows weak energy dependence between 13A and 30A GeV/ c .

4.1.3 (CP) Femtoscopy analysis in the 20% most central Be+Be collisions at 150A GeV/ c

The nature of the quark-hadron transition can be studied via Bose-Einstein correlations (femtoscopy), as the investigation of the femtoscopic correlation functions in heavy ion reactions reveals the space-time structure of hadron production from the sQGP. With the use of Lévy-type sources, one can describe the measured correlation functions and discuss the measurement of the Lévy source parameters (α , λ and R) as a function of average pair transverse mass (m_T).

Recent results [20,21], shown in Figs. 10 and 11, on the first Lévy-HBT analysis in Be+Be at 150A GeV/ c were well received at the main conference of the field, the XIV Workshop on Particle Correlations and Femtoscopy in Dubna. The 20% most central events were analyzed, and momentum correlations of identified pions (positive and negative pairs separately) at mid-rapidity were measured. The correlation functions could be described with the assumption of Lévy sources in a statistically acceptable manner, enabling the interpretation of the fit parameters. Below details are given on these results.

The Lévy stability parameter α describes the shape of the source. As shown in the *upper left* plot of Fig. 10, the measured α parameter has no significant transverse mass (m_T) dependence, and the pion producing source in 150A GeV/c Be+Be collision appears not to be Gaussian (corresponding to $\alpha = 2$). These results are similar to those measured by PHENIX in the 30% most central Au+Au collisions at $\sqrt{s_{NN}} = 200$ GeV [22]. Furthermore, α was conjectured to be related to one of the critical exponents (the so-called correlation exponent η), and thus may shed light on the location of the critical endpoint (CP) on the QCD phase diagram. The measured α is far from the CP conjecture ($\alpha = 0.5$), as shown in the *upper left* plot of Fig. 10, calling for investigations at other energies and in other collision systems.

The correlation strength λ is related to the core-halo ratio, where the core contains pions created primordially or from short lived resonances, while the halo consists of the decay products of longer lived resonances. In previous RHIC and SPS results, see e.g. Ref. [23] (STAR) or Ref. [24] (NA44) or Ref. [25] (NA49), different m_T dependences were found. The NA61/SHINE results in the *upper right* plot of Fig. 10 show no significant m_T dependence, similar to NA44 and NA49 results.

The Lévy scale R corresponds to the femtoscopic scale of the system, i.e. the length of homogeneity. From a simple hydrodynamical picture one obtains an $R \approx 1/\sqrt{m_T}$ type of transverse mass dependence, creating a decreasing trend in m_T , generally attributed to transverse flow. The new Be+Be results, shown in the *bottom* plot of Fig. 10, indicate that R weakly decreases with m_T , showing a hydro-type of transverse flow effect. This behavior was not only seen in heavy ion experiments, but also in proton-proton collisions at RHIC - see e.g. Ref. [26] (STAR).

The Lévy parameters (α , R and λ) are correlated, and especially in a low statistics dataset, it is hard to determine them precisely. One might be able to reduce this correlation and the statistical uncertainty of the parameters, if one fixed one of the three parameters to a well defined value. One option is fixing α to a weighted average of the four α values obtained in free parameter fits performed in each K_T (average pair transverse momentum) bin, with the assumption of transverse mass independence of α . The other option is fixing R with the following equation motivated by hydrodynamical predictions of the particle emission homogeneity length (HBT radii) of expanding fireballs:

$$R(m_T) = \frac{A}{\sqrt{1 + m_T/B}}. \quad (1)$$

By fixing R one can more precisely determine the value α , which is the most important variable in this analysis with respect to the critical point search.

Figure 11 shows fits with α or R fixed to a given (in case of R , m_T dependent) value, as detailed above. When comparing the three different fits (free parameter fit, fixed α fit, fixed R fit), it is visible that they are compatible within statistical uncertainties, which are however significantly reduced in case of the fixed α or R fits.

4.1.4 (CP) Intermittency of protons in Ar+Sc collisions at 150A GeV/c

In the 2018 Status Report [27], preliminary results were reported on proton intermittency analysis in Ar+Sc collisions at 150A GeV/c. Presently an attempt is being made to improve

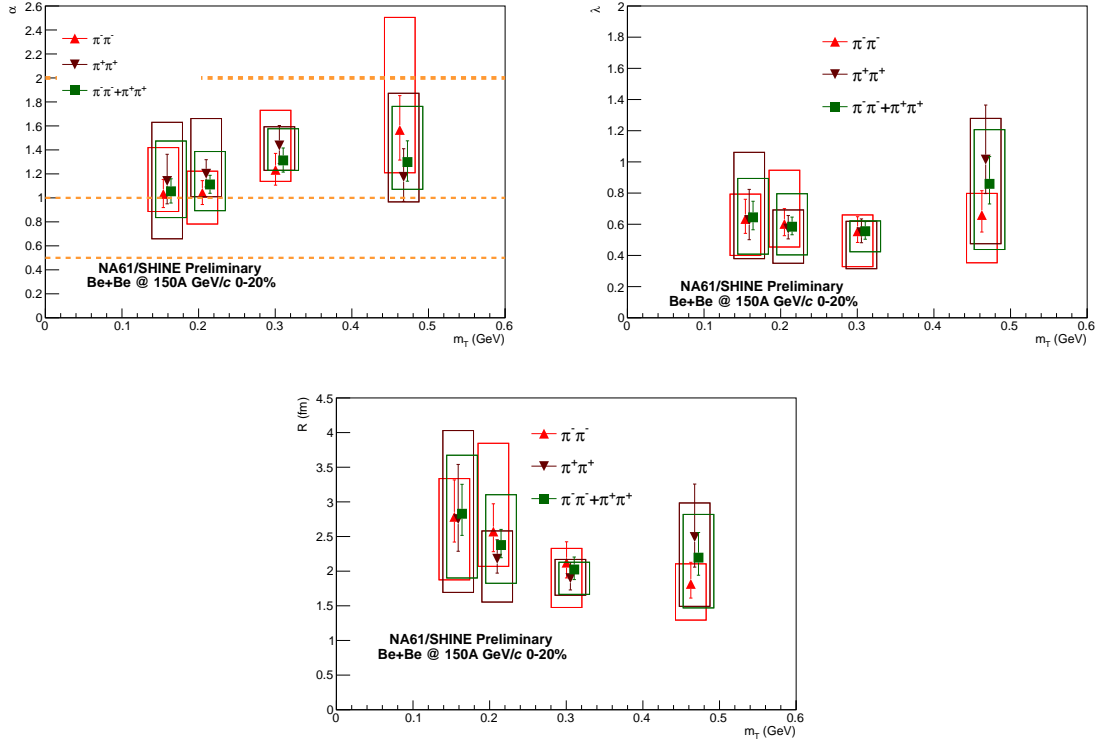


Figure 10: Lévy stability parameter as function of collision energy for p+p, Be+Be, Ar+Sc, and Pb+Pb/Au+Au collisions. α , Lévy correlation strength λ and Lévy scale parameter R versus m_T . Preliminary results for the 20% most central Be+Be collisions at 150 A GeV/c.

the estimate of the statistical significance of this result. This issue is non-trivial because of strong bin-by-bin correlations in the correlator $\Delta F_2(M)$, but of high importance in view of the possible interpretation of this result as related to the presence of the critical point [28]. The results of this analysis were presented for the first time at the 2019 European Physical Society Conference on High Energy Physics [29].

Figure 12 (left) shows the values of $\Delta F_2(M)$ for 10-15% central Ar+Sc collisions at 150 A GeV/c; original sample data values and their bootstrap standard errors are plotted against confidence intervals (68-95-99.7%) of the $\Delta F_2(M)$ distributions obtained from 1000 bootstrap resamplings of the analyzed events. Figure 12 (right) compares the experimental $\Delta F_2(M)$ values against the $\Delta F_2(M)$ values obtained from uncorrelated proton background with the same inclusive characteristics as the original Ar+Sc events.

Based on the observed $\Delta F_2(M)$ confidence intervals for Ar+Sc experimental data, one can conclude that $\sim 95\%$ of values are above the zero line, indicating a statistically significant separation of SSFMs of real data from mixed events (background). Figure 12 (right) demonstrates that only 1 – 5% of uncorrelated proton background events produce a $\Delta F_2(M)$ signal as strong as the one observed in experimental data. One may therefore assign a 95% statistical significance to the observed experimental result being non-random.

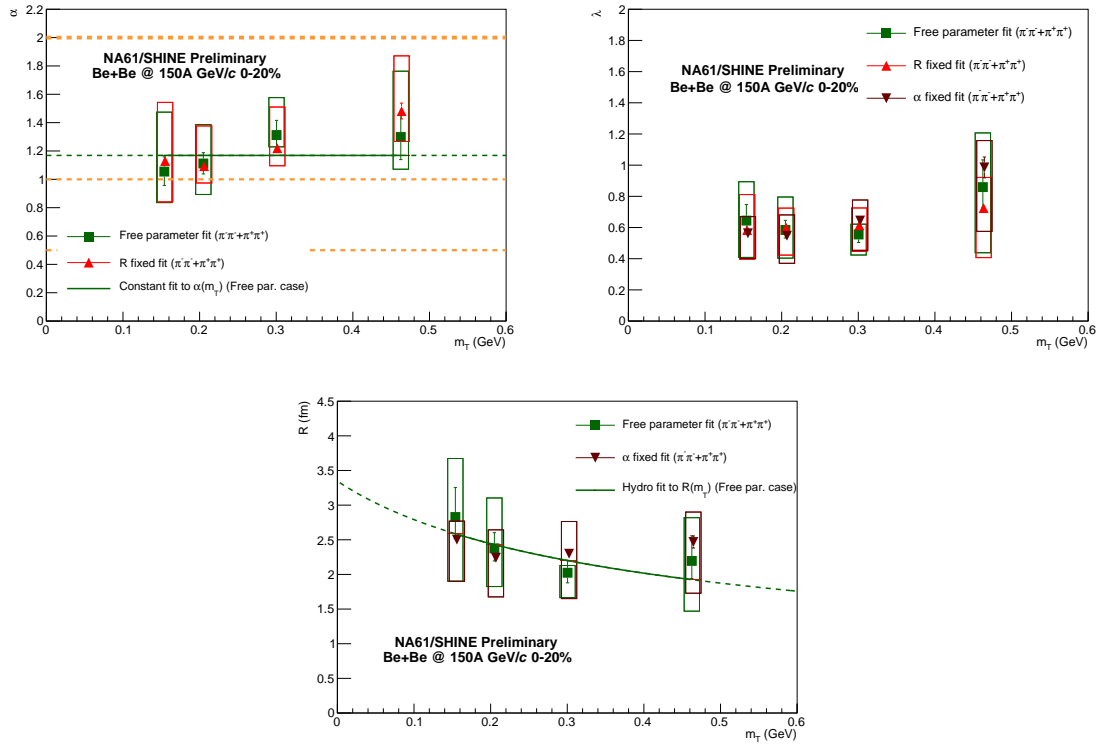


Figure 11: Lévy parameter α , λ and R versus m_T . Comparison between free parameter fit, fit with α fixed and fit with R fixed. Preliminary results for the 20% most central Be+Be collisions at 150A GeV/c.

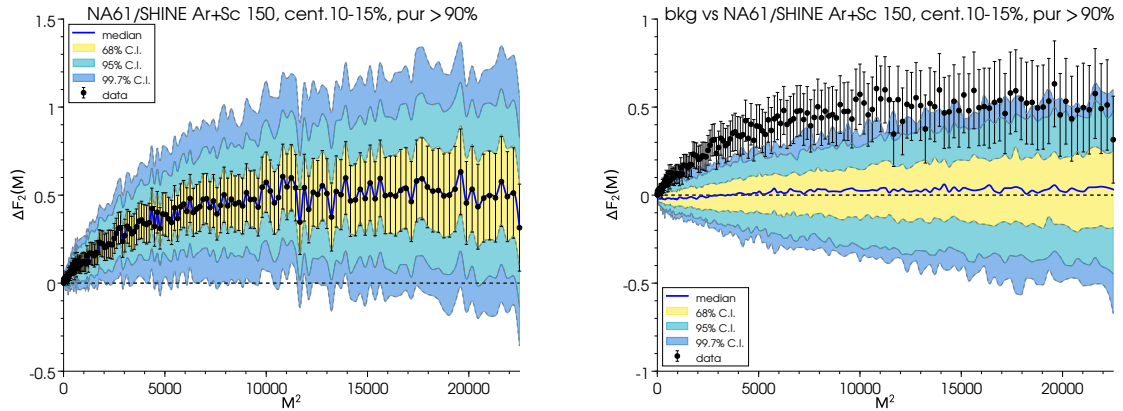


Figure 12: (left) $\Delta F_2(M)$ original sample values for 10-15% central Ar+Sc collisions at 150A GeV/c (black points); error bars correspond to bootstrap standard error; colored bands indicate bootstrap confidence intervals; solid blue line gives the median value of bootstrap samples. (right) The same experimental $\Delta F_2(M)$ values (black points) compared to the $\Delta F_2(M)$ results for simulated random background protons.

4.1.5 (O) Final results on ϕ meson production in p+p collisions

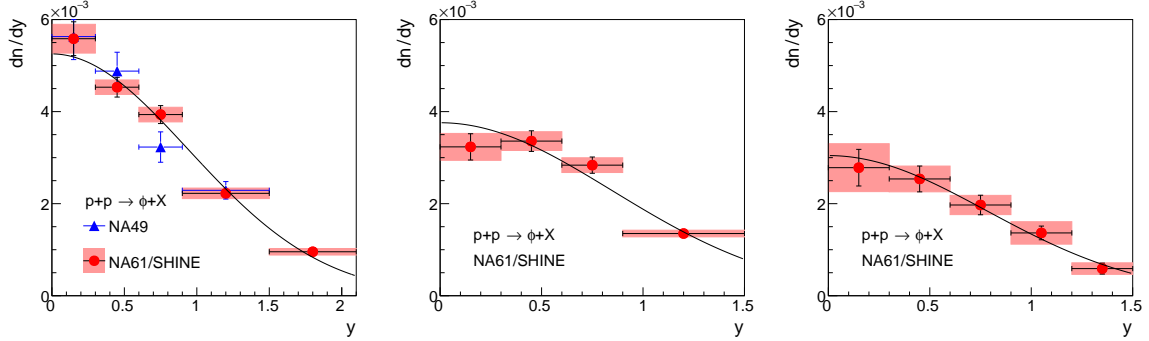


Figure 13: Final rapidity distributions of ϕ mesons produced in p+p collisions at beam momenta (from left to right) 158, 80 and 40 GeV/c. NA49 points (triangles) come from Ref. [30]. Solid curves are Gaussian fits.

Final results on the measurements of ϕ meson production in p+p interactions have recently been submitted for publication [31]. They include the first ever measured double differential spectra of ϕ mesons as a function of rapidity and transverse momentum for proton beam momenta of 80 GeV/c and 158 GeV/c, as well as single differential spectra of y or p_T for beam momentum of 40 GeV/c. Figure 13 presents p_T integrated rapidity distributions of ϕ mesons measured by NA61/SHINE in comparison with single differential results from NA49 [30].

These measurements may serve as reference for analogous measurements in Pb+Pb collisions to infer about strangeness-related phenomena in heavy ion collisions. Furthermore, they provide important input to improve hadron production models at CERN SPS energies, in the sector of strangeness production.

Comparing to the earlier, preliminary version of these results, reported in Ref. [32] and presented e.g. at Quark Matter 2018 [33], background reduction around ϕ midrapidity and background parametrization in the invariant mass fits were improved [31]. This resulted in better agreement with NA49 results at midrapidity.

4.1.6 (O) $K^*(892)^0$ meson production in p+p interactions at 40 and 80 GeV/c

The first NA61/SHINE measurement of $K^*(892)^0$ meson production via its $K^+ \pi^-$ decay mode in inelastic p+p collisions at beam momentum 158 GeV/c ($\sqrt{s_{NN}} = 17.3$ GeV) was obtained in 2018 [34, 35] and presented also in the last Status Report. This year new preliminary results were added for p+p collisions at 40 and 80 GeV/c [36]. The *template* method was used to extract raw $K^*(892)^0$ signals. In this method the background is described as a sum of two components: mixed events and Monte Carlo generated templates which describe the contribution of $K^+ \pi^-$ pairs coming from sources other than the $K^*(892)^0$. For the studied resonance, the *template* method was found to be much more effective in estimating the background than the *standard* procedure relying on mixed events only.

Figure 14 presents the mid-rapidity transverse mass spectra of $K^*(892)^0$ mesons produced in inelastic p+p collisions at 40, 80, and 158 GeV/c. The rapidity spectra obtained by integrating and extrapolating the transverse momentum distributions are shown in Fig. 15.

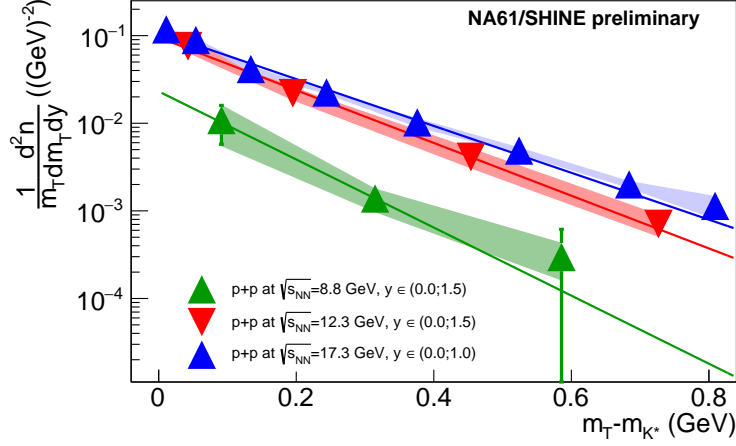


Figure 14: Preliminary results on mid-rapidity transverse mass spectra of $K^*(892)^0$ mesons produced in inelastic p+p collisions at 40, 80, and 158 GeV/c.

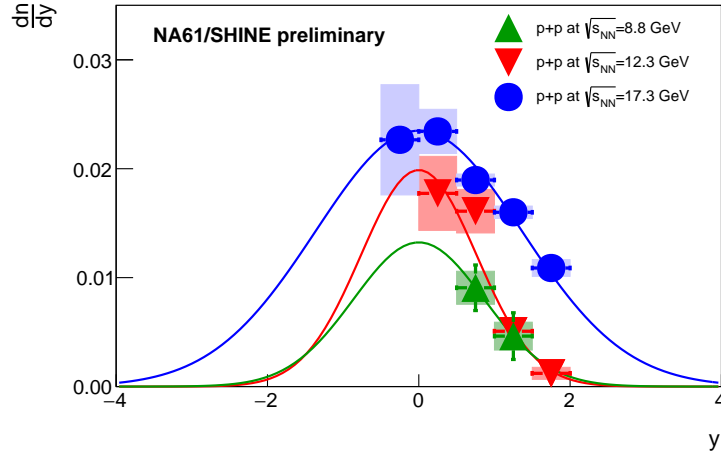


Figure 15: Preliminary results on rapidity spectra of $K^*(892)^0$ mesons produced in inelastic p+p collisions at 40, 80, and 158 GeV/c. For 40 and 80 GeV/c the results were obtained by averaging over a wide transverse momentum range ($0 < p_T < 1.5$ GeV/c), whereas for 158 GeV/c p_T -extrapolated and integrated ($0 < p_T < \infty$) results are shown.

The mean multiplicities of $K^*(892)^0$ mesons in full phase-space (158 GeV/c) or in $0 < p_T < 1.5$ GeV/c (40 and 80 GeV/c) were obtained from summing the measured points and adding the contribution from a Gaussian fit in the unmeasured region (lines in Fig. 15). For 158 GeV/c the point with $y < 0$ was calculated only to check the symmetry of the rapidity distribution and was not included in the procedure of mean multiplicity determination. The numerical values of the mean multiplicities of $K^*(892)^0$ mesons are presented in Table 1.

$\sqrt{s_{NN}}$	NA61/SHINE preliminary	NA49 [37]
8.8	$0.0285 \pm 0.0031 \pm 0.0046$	-
12.3	$0.0381 \pm 0.0054 \pm 0.0037$	-
17.3	$0.0806 \pm 0.0006 \pm 0.0026$	$0.0741 \pm 0.0015 \pm 0.0067$

Table 1: Mean multiplicities of $K^*(892)^0$ mesons produced in inelastic p+p collisions at 40, 80, and 158 GeV/c. For NA61/SHINE 40 and 80 GeV/c, as well as NA49 [37] 158 GeV/c data. The first uncertainty is statistical and the second is systematic.

The new $K^*(892)^0$ results of NA61/SHINE were compared with predictions of the statistical Hadron Resonance Gas model [38,39] in Canonical (CE) and Grand Canonical (GCE) formulations (Fig. 16). At 158 GeV/c the GCE model provides a very good description of $K^*(892)^0$ production in the small p+p system. The CE model also agrees provided that the ϕ meson is excluded from the fits. Please see Refs. [34–36] for comparisons of 158 GeV/c data with Hadron Resonance Gas models of different authors.

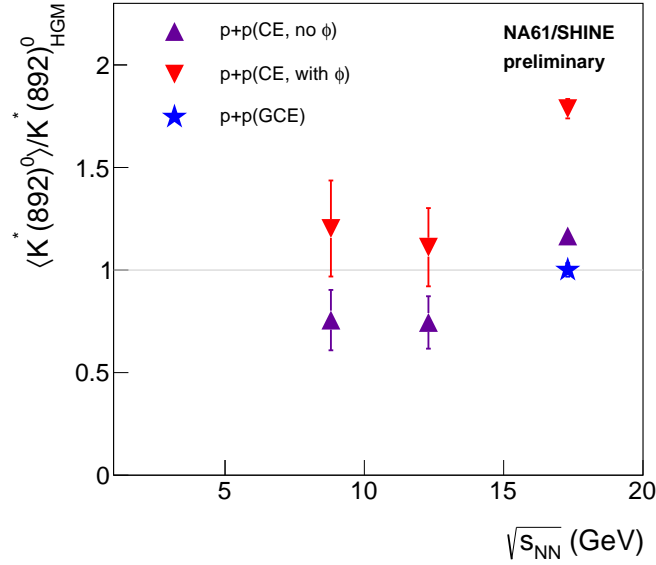


Figure 16: Preliminary results on mean multiplicities of $K^*(892)^0$ mesons produced in p+p collisions compared to Hadron Gas Model predictions [38,39]. Statistical and systematic uncertainties of $\langle K^*(892)^0 \rangle$ were added in quadrature.

4.1.7 (O) Ξ^+ spectra and Ξ^+/Ξ^- ratios in p+p interactions at 158 GeV/c

Hyperons are excellent probes of the dynamics of proton-proton interactions as constituent strange quarks are not present in the initial state of this process. Therefore hyperon production has been studied in a long series of experiments in elementary hadron+hadron interactions. However, the experimental situation in this field remains inconclusive.

This report presents new data [10] from p+p collisions on Ξ^+ anti-hyperon production. The

event sample consists of 53 million registered interaction trigger events obtained at 158 GeV/c beam momentum corresponding to $\sqrt{s_{NN}} = 17.3$ GeV/c. The results refer to primary Ξ^+ produced in strong and electromagnetic processes and are corrected for detector geometrical acceptance and reconstruction efficiency.

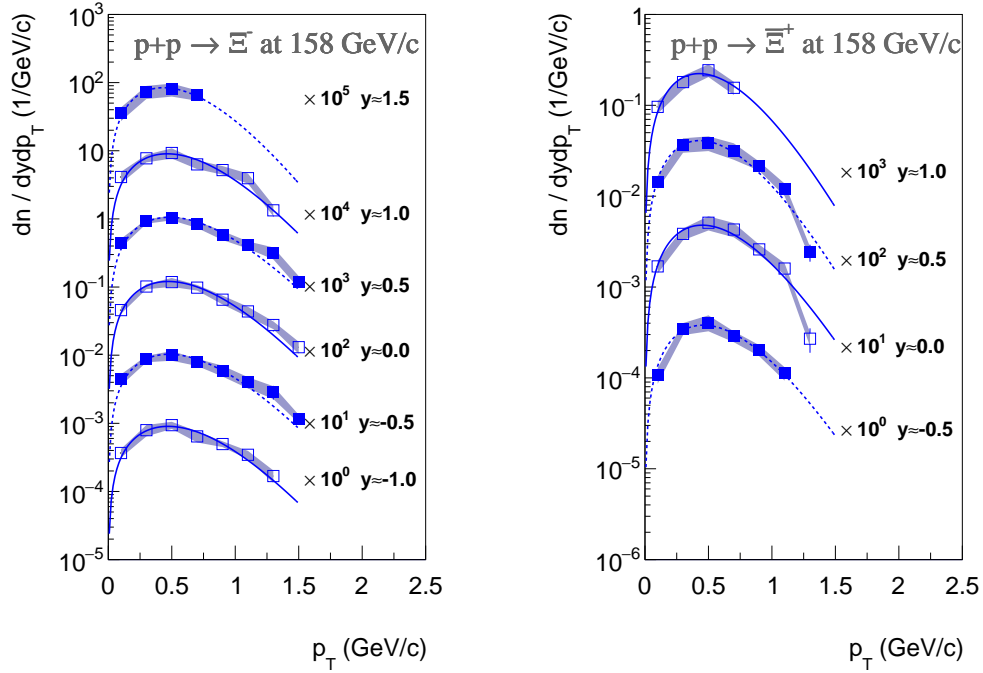


Figure 17: Preliminary results on transverse momentum spectra of Ξ^- (left) and Ξ^+ (right) produced in inelastic p+p interactions at 158 GeV/c in consecutive rapidity bins. Results are scaled for better separation, shaded bands present systematic uncertainty.

To reduce the background in the invariant mass distribution several selection criteria were applied and about half of the background is removed with these cuts, with the signal effectively unchanged.

The invariant mass spectrum of Ξ candidates was fitted with a function consisting of a Lorentzian for the signal and a polynomial (up to 4th order) for the background. The same analysis was performed on simulated events in order to obtain corrections for geometrical acceptance and reconstruction efficiency.

Preliminary results derived from two dimensional spectra (y vs p_T) are presented as transverse momentum distributions in bins of rapidity in Fig. 17 (the results for Ξ^- were already presented in the last Status Report, the results for Ξ^+ were released this year [10]). Statistical uncertainties are shown as vertical bars and preliminary estimates of systematic uncertainty are indicated by shaded bands. The blue lines present results of exponential fits to the data binned in m_T .

The presented p_T spectra were used to calculate the rapidity spectrum of Ξ^+ production as the sum of measured points and extrapolation to the unmeasured region of p_T . The result

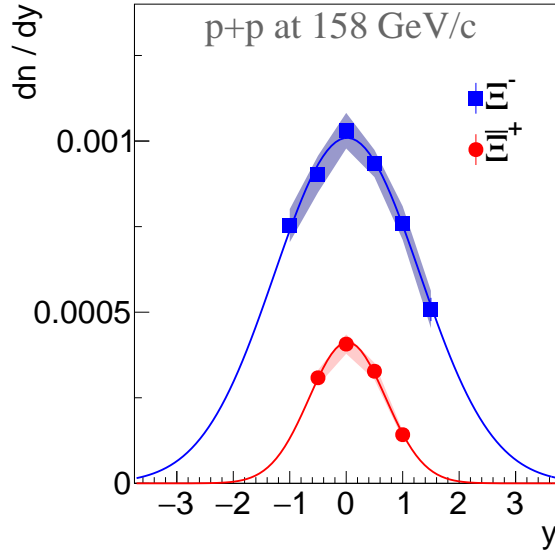


Figure 18: Preliminary results on rapidity spectrum of Ξ^+ (red) and Ξ^- (blue) hyperons produced in inelastic p+p interactions at 158 GeV/c fitted by a Gaussian function (lines).

is displayed in Fig. 18 together with the Ξ^- spectrum released last year. Vertical bars show statistical, the shaded band systematic uncertainties. The rapidity distribution was fitted by a Gaussian function for extrapolation into the unmeasured regions. Summing of the data points and extrapolation of the fitted function resulted in the mean multiplicity $\langle \Xi^+ \rangle = 0.00079 \pm 0.00002 \pm 0.00010$. For a comparison, the mean multiplicity of Ξ^- , reported last year, was equal to $0.0033 \pm 0.0001 \pm 0.0006$.

The newest results on Ξ^+ and Ξ^+/Ξ^- spectra in p+p interactions at 158 GeV/c were presented for the first time at the 2019 conference on Strangeness in Quark Matter [10].

4.1.8 (O) Pentaquark $\Xi(1860)^{--}$ search in p+p collisions at 158 GeV/c

The NA49 Collaboration presented evidence for the existence of a narrow $\Xi^- \pi^-$ baryon resonance with mass of 1.862 ± 0.002 GeV/ c^2 and width below the detector resolution. The significance was estimated to be 4.0σ . This state was a candidate for the hypothetical exotic $\Xi_{\frac{3}{2}}^{--}$ baryon with $S=-2$, $I=\frac{3}{2}$ and a quark content of $(dsds\bar{u})$. At the same mass a peak was observed in the $\Xi^- \pi^+$ spectrum which is a candidate for the $\Xi_{\frac{3}{2}}^0$ member of this isospin quartet with a quark content of $(dsus\bar{d})$. The corresponding anti-baryon spectra also showed enhancements at the same invariant mass [40].

Recently, a similar analysis with much larger statistics was performed by NA61/SHINE [10]. The first step in the analysis was the search for Λ candidates, which were then combined with the π^- to form the Ξ^- candidates. Next the $\Xi_{\frac{3}{2}}^{--}$ ($\Xi_{\frac{3}{2}}^0$) were searched for in the Ξ^-

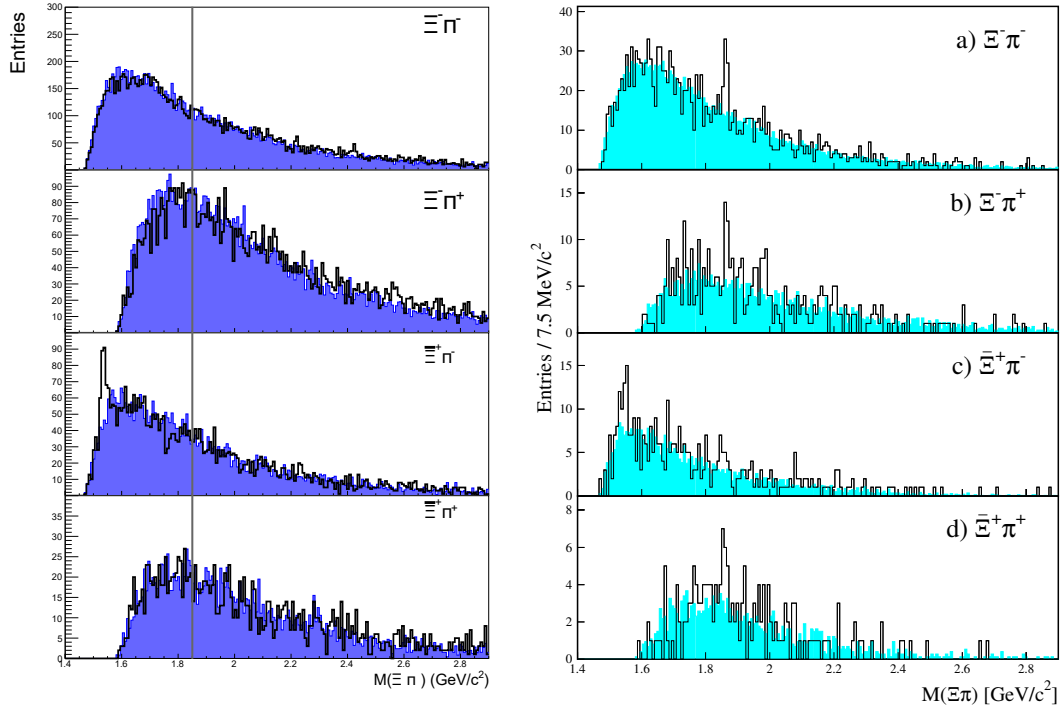


Figure 19: *Left:* NA61/SHINE invariant mass spectra after selection cuts for $\Xi^- \pi^-$, $\Xi^- \pi^+$, $\Xi^+ \pi^-$ (note that the $\Xi(1530)^0$ state is also visible) and $\Xi^+ \pi^+$. The shaded histograms are the normalised mixed-event backgrounds. Gray line marks the location where an indication of a pentaquark signal was observed by the NA49 Collaboration. NA61/SHINE results [10] were obtained for 53M interaction trigger events (33M after all event cuts). *Right:* Similar plots but obtained by NA49 [40]. In NA49 6.5M recorded events (3.75M after event cuts) were used.

$\pi^- (\Xi^- \pi^+)$ invariant mass spectrum, where the $\pi^- (\pi^+)$ are primary vertex tracks. An analogous procedure was followed for the antiparticles.

To search for the exotic $\Xi_{3/2}^{--}$ state the selected Ξ^- candidates were combined with primary π^- tracks. The resulting $\Xi^- \pi^-$ invariant mass spectrum is shown in Fig. 19 (top, left). The shaded histogram is the mixed-event background, obtained by combining the Ξ^- and π^- from different events and normalising to the number of real combinations. The complete list of invariant mass distributions, measured recently by NA61/SHINE ($\Xi^- \pi^-$, $\Xi^- \pi^+$, $\Xi^+ \pi^-$, $\Xi^+ \pi^+$), is shown in Fig. 19 (left). In addition to the described cuts, a lower cut of 3 GeV/c was imposed on the π^+ momenta to minimize the large proton contamination. Blue histograms show normalised mixed-event backgrounds. One sees that the data overlap with the mixed-event backgrounds in the mass window 1.848 – 1.870 GeV/c² where the NA49 signal was observed; see Fig. 19 (right). Finally a narrow peak of $\Xi(1530)^0$ is observed in the invariant mass of $\Xi^+ \pi^-$. The yield of observed $\Xi(1530)^0$ scales with the number of events compared to NA49 results.

In summary, this NA61/SHINE analysis of p+p data, with ≈ 10 times higher statistics, does

not confirm the NA49 indication of $\Xi_{\frac{3}{2}}^{--}$, $\Xi_{\frac{3}{2}}^0$ and their antiparticles. All four invariant mass distributions shown in Fig. 19 do not show significant signals in the mass window where a pentaquark candidate was observed previously.

4.1.9 (O) Performance results from Vertex Detector for Xe+La at 150A GeV/c

The performance results are based on the Xe+La data for beam momentum of 150A GeV/c taken in 2017. The SAVD tracks matched to TPC tracks are used to search for the $D^0 + \overline{D}^0$ signal. In the analysis presented here, the PID information was derived from dE/dx signals which were not yet fully calibrated. Each SAVD track is paired with another SAVD track and is assumed to be either a kaon or a pion, unless the track identity is known from the dE/dx information. The combinatorial background is several orders of magnitude higher than the $D^0 + \overline{D}^0$ signal due to the low yield of charm particles. Five cuts were applied in order to reduce the large background. The cut parameters were chosen to maximize the signal to noise ratio (SNR) of the reconstructed $D^0 + \overline{D}^0$ peak and were determined from simulations [41]. These cuts are:

- (i) cut on the track transverse momentum, $p_T > 0.34 \text{ GeV}/c$;
- (ii) cut on the track impact parameter, $d > 34 \mu\text{m}$;
- (iii) cut on the longitudinal distance between the D^0 decay vertex candidate and the primary vertex, $V_z > 475 \mu\text{m}$;
- (iv) cut on the impact parameter D of the back-extrapolated D^0 candidate momentum vector, $D < 21 \mu\text{m}$;
- (v) and finally a cut on the distance of the closest approach of the two tracks of the pair, $\text{DCA} < 21 \mu\text{m}$.

The d and D parameters are defined as the shortest distance between the primary vertex and the track line of a single track and D^0 candidate, respectively. Note, that the last four cuts are based on information delivered by the SAVD. The cut values were first developed using Monte-Carlo simulations and refined on real data.

Figure 20 shows the invariant mass distribution of unlike charge sign daughter candidates with the applied cuts. One observes a peak emerging at $1.87 \text{ GeV}/c^2$, which is consistent with production of $D^0 + \overline{D}^0$. The invariant mass distribution was fitted (red line) using an exponential function to describe the background and a Gaussian to describe the $D^0 + \overline{D}^0$ signal contribution. From the fit one finds the width of the peak to be $10 \text{ MeV}/c^2$, consistent with the value obtained in simulations taking into account instrumental effects. The total yield amounts to about 50 with a $\pm 3\sigma$ integrated SNR of 4.0. Further improvement of this result is expected after introduction of dE/dx calibrations and residual distortion corrections.

The same strategy of background suppression as that described above can be applied for reconstruction of K_S^0 and Λ^0 particles. Figure 21 (left) shows the invariant mass distribution in the region of the K_S^0 mass for unlike charge sign pairs assigning the π mass to both tracks of the pair. The result was obtained for 1.1×10^6 collisions of Xe+La at the beam momentum of 150A GeV/c. No event selection was applied. A clear K_S^0 peak is seen at $499.61 \text{ MeV}/c^2$

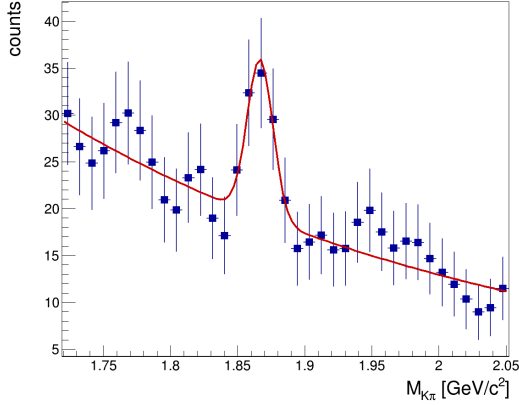


Figure 20: Invariant mass distribution of unlike charge sign π, K decay track candidates in Xe+La collisions at 150A GeV/c taken in 2017.

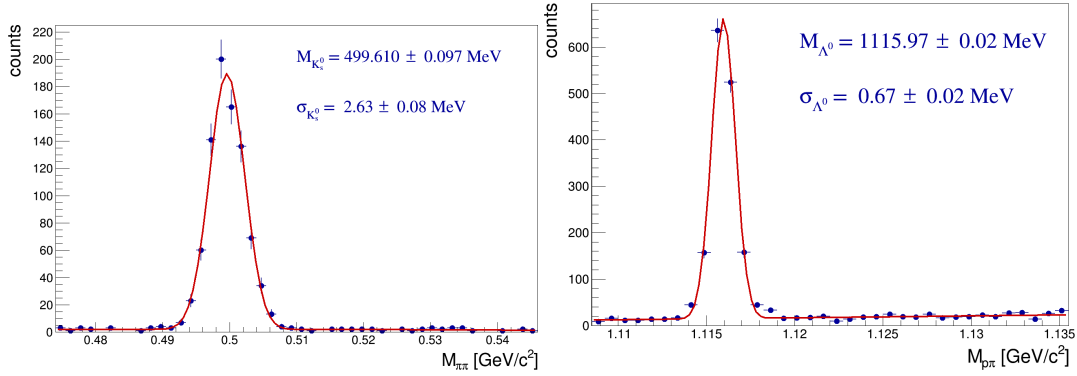


Figure 21: Invariant mass distribution of unlike charge sign π, π decay (*left*) and π, p (*right*) track candidates in Xe+La collisions at 150A GeV/c.

with a width of $2.63 \text{ MeV}/c^2$. For the same data Fig. 21 (*right*) presents the invariant mass distribution in the region of the Λ mass for the unlike charge sign pairs assigning the proton mass to the positively charged track and the π^- mass to the negatively charged track of the pair. As in the case of K_S^0 a clear Λ peak appears at mass of $1115.682 \text{ MeV}/c^2$ with a width of $0.67 \text{ MeV}/c^2$. In both figures the red line represents a fit with a Gaussian function to account for the signal plus a second order polynomial to account for the remaining background. The cut parameters were not optimized to maximize the signal significance. In this analysis rather arbitrary cuts were used just to demonstrate the ability of K_S^0 and Λ reconstruction. The width of the Λ peak is significantly smaller than the width of the K_S^0 peak, as expected. The reconstructed masses exceed the known values for K_S^0 and Λ by $2 \text{ MeV}/c^2$ and $0.67 \text{ MeV}/c^2$, respectively. Although the shifts are small they are much larger than the statistical uncertainty and are presumably related to the limited control of the absolute value of the magnetic field. The observed discrepancy can be used to calibrate the absolute strength of the magnetic field. Applying a linear extrapolation of the apparent K_S^0 and Λ mass shift to the D^0 mass region one expects a shift on the level of $10 \text{ MeV}/c^2$. This prediction agrees very well with the location of the D^0 peak presented in Fig. 20.

4.2 New results for neutrino physics

The NA61/SHINE collaboration has recently obtained and released reference measurements obtained for long-baseline neutrino oscillation experiments at J-PARC and FNAL.

4.2.1 Final results on hadron emission from the T2K replica-target (J-PARC)

A paper devoted to measurements of double differential yields of π^+ , π^- , K^+ , K^- and protons emitted from the surface of a 90 cm-long carbon target (T2K replica) with incoming 31 GeV/c protons was recently published [42].

Yields of K^+ , K^- and proton were obtained and published for the first time, while π^+ and π^- yields were measured with improved precision compared to the previously published NA61/SHINE results [43].

These newly published measurements are crucial for further reducing the hadron production component of the T2K (anti)neutrino flux error [44], which is the dominant component in the flux uncertainty. Expected reduction of the flux uncertainties down to about 5% [45] will directly improve measurements of the (anti)neutrino-nucleus cross sections as well as of the (anti)neutrino oscillation parameters in T2K.

4.2.2 Production cross section of p+C interactions at 31 GeV/c for T2K (J-PARC)

Complementary data with the T2K replica target were also taken using the maximal magnetic field. Analysis of the recorded 1.2 M events aims to measure the fraction of non-interacting beam particles passing through the target, i.e. the beam survival probability. The maximum magnetic field is needed to bend the high energy beam particles, 31 GeV protons, to the TPCs for proper reconstruction. Having a measure of the beam survival probability, P_{survival} , and using the relation:

$$P_{\text{survival}} = e^{-Ln\sigma_{\text{prod}}}, \quad (2)$$

where L is the length of the particle trajectory in the target and n is the number of carbon atoms per unit volume, the production cross section σ_{prod} can be estimated. Note that any interaction in which new hadrons are produced is regarded as production.

Analysis of these data is ongoing. The corresponding simulations with the FLUKA2011.2c.5 package are already produced, while GEANT4 10.04.03 predictions are under development.

4.2.3 Cross section of p+Be/C/Al interactions at 60 and 120 GeV/c (FNAL)

During the 2016 data collection, NA61/SHINE recorded interactions of protons on thin carbon, beryllium, and aluminum targets using beam momenta of 60 GeV/c and 120 GeV/c. Interactions were recorded with all three targets at 60 GeV/c, while interactions on thin carbon and beryllium targets were recorded at 120 GeV/c. Measurements of proton inelastic

and production cross sections have recently been completed using these data sets and submitted for publication in *Phys. Rev. D* [46].

The production cross section with a proton beam at 120 GeV/c was measured for the first time with a precision of about 6% (8%) for p + C (p + Be) including statistical, systematic, and model uncertainties. At 60 GeV/c, the measured production cross sections are comparable to previous results for p + C and p + Al, and the precision was improved to about 3%. The production cross section of p + Be at 60 GeV/c was measured for the first time with a precision of about 4% including statistical, systematic, and model uncertainties.

The inelastic cross section with a proton beam at 120 GeV/c was measured for the first time with a precision of about 6% (8%) for p + C (p + Be) including statistical, systematic, and model uncertainties. For the inelastic production cross section of the proton beam at 60 GeV/c, reasonable agreement with a previous measurement was found.

The measurements are summarized in Figure 22.

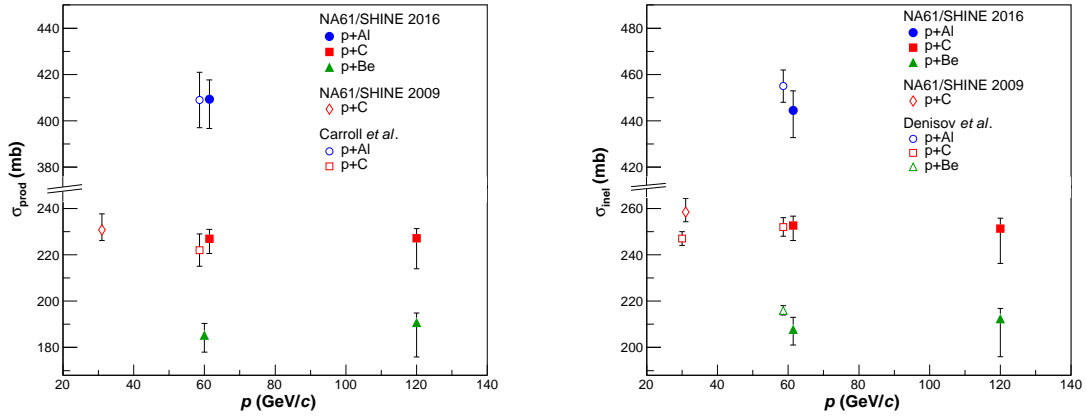


Figure 22: (Left) Summary of production cross section measurements. The results are compared to former results by Carroll *et al.* [47]. (Right) Summary of inelastic cross section measurements. The results are compared to former results by Denisov *et al.* [48].

4.2.4 Hadron spectra in π^+ +Be/C interactions at 60 GeVc (FNAL)

In the momentum range that is relevant for the current and future long-baseline neutrino program at Fermilab, there is very little existing data on the spectra of hadrons that are produced by pions that re-interact in the neutrino target. An analysis of the interactions of 60 GeV/c π^+ with thin, fixed carbon and beryllium targets has recently been completed [49] using data collected in NA61/SHINE in 2016. A paper has been finalized recently and submitted for publication in *Phys. Rev. D* [50]. Integrated production and inelastic cross sections were measured for both of these reactions. In an analysis of strange, neutral hadron production, differential production multiplicities of K_s^0 , Λ and $\bar{\Lambda}$ were measured. Lastly, in an analysis of charged hadron production, differential production multiplicities of π^+ , π^- , K^+ , K^- and protons were measured. These measurements will enable long-baseline neutrino

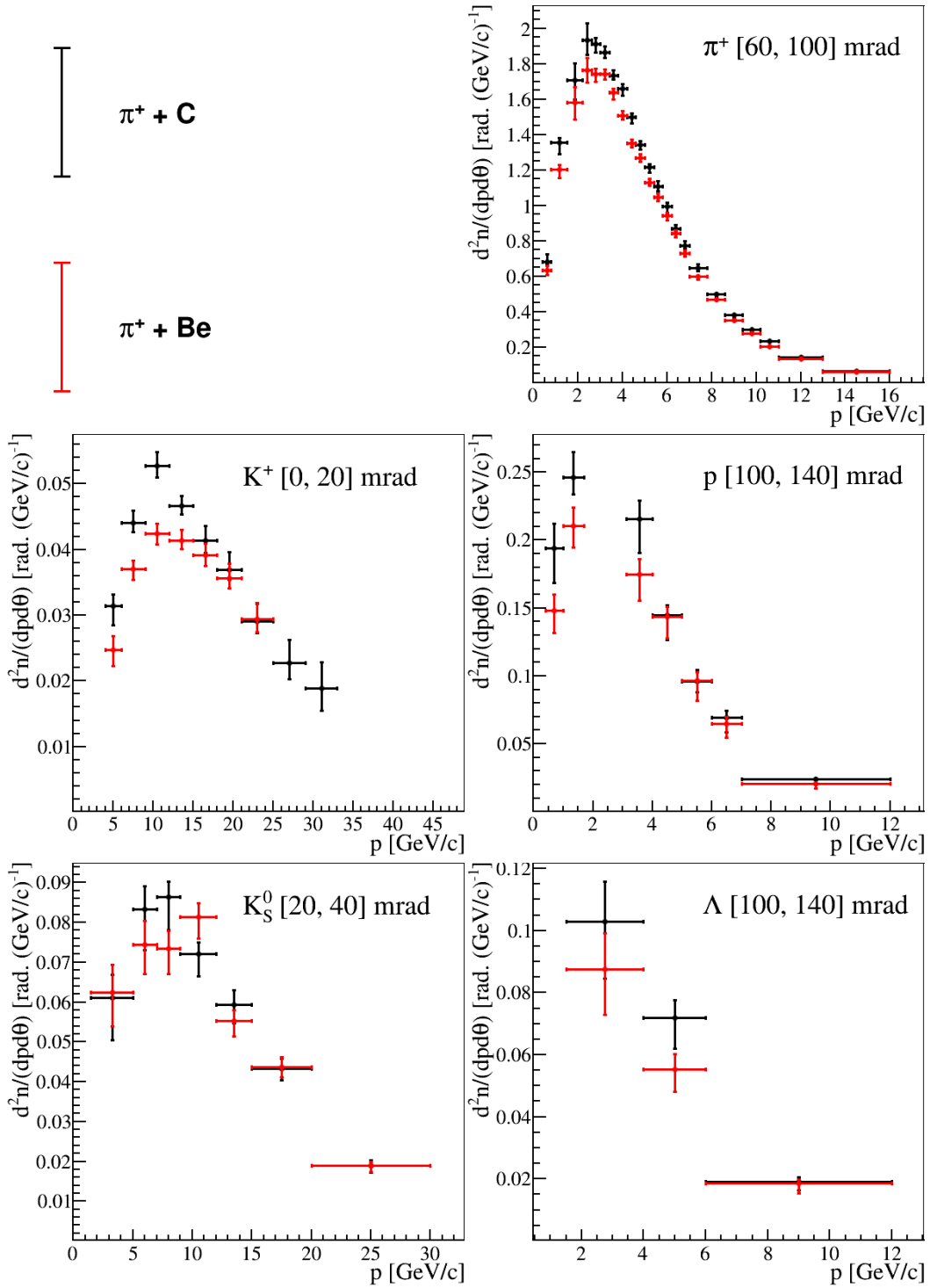


Figure 23: Measurements of momentum spectra from π^+ + C at 60 GeV/c and π^+ + Be at 60 GeV/c interactions are shown for produced π^+ , K^+ , proton, K_S^0 , and Λ for selected representative angular bins. The error bars represent total uncertainties except for the normalization uncertainty.

experiments to better constrain predictions of their neutrino flux in order to achieve better precision on their neutrino cross section and oscillation measurements. A comparison of the results for the carbon and beryllium targets for a few selected bins are shown in Figure 23.

In addition to the integrated cross section measurements discussed in Section 4.2.3, analysis is currently in progress to extract new hadron production spectra from those datasets as well.

4.3 New results for cosmic-ray physics

NA61/SHINE measurements for cosmic-ray physics include measurements needed to improve simulations of cosmic-ray induced air showers (CR-A) and understanding of cosmic-ray propagation in the Galaxy (CR-G).

4.3.1 \bar{p} spectra in $\pi^- + C$ interactions at 158 and 350 GeV/c (CR-A)

The vast majority of hadronic interactions in cosmic-ray induced air showers are π +air interactions and the muons observed by particle detectors of surface detectors mostly originate from decays of pions that were produced in pion-air interactions at equivalent beam energies below a TeV [51–53]. Therefore, new data with pion beams at 158 and 350 GeV/c on a thin carbon target (as a proxy for nitrogen) were collected in 2009 by the NA61/SHINE experiment and the production spectra of charged hadrons and identified particles (π^\pm , K^\pm , $p(\bar{p})$, $\Lambda(\bar{\Lambda})$, K_S^0 , K^{*0} , ω and ρ^0) [54–59] were previously reported. The preliminary measurements of \bar{p} production in $\pi^- + C$ interactions had sizeable systematic uncertainties due to a model-dependent correction for the feed-down of antiprotons from weak decays, mainly from $\bar{\Lambda} \rightarrow \bar{p} + \pi^-$. This section presents an update of this measurement with a data-driven correction for the feed-down. For this purpose first $\bar{\Lambda}$ production in $\pi^- + C$ interactions [59] was measured and then the model correction was re-weighted accordingly as described in [60]. The result is shown in Fig. 24 and compared to predictions of hadronic interaction models used in air shower simulations. As can be seen, none of the most recent versions of the models describes the data well. The older version 1.99 of EPOS, however, gives a very good description of the data. The current “LHC” version of this model clearly overproduces anti-protons. Hence the enhanced transfer to the hadronic cascade and the corresponding larger amount of muon production in this model is strongly disfavored by the new measurement. On the other hand, all the remaining models under-produce anti-protons and thus it can be conjectured that an increase of anti-baryon production in these models to match our measurement could alleviate the muon deficit reported by air shower experiments.

These updated corrections to the anti-proton spectra conclude the extensive NA61/SHINE studies of the interactions of pion projectiles and a paper summarizing all results will be submitted this year.

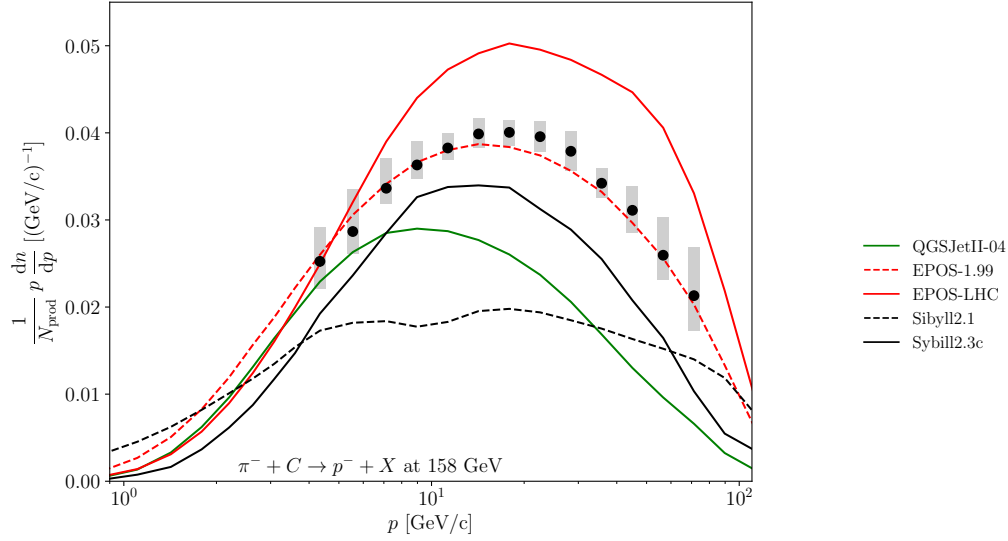


Figure 24: Comparison of the p_T -integrated \bar{p} momentum spectrum in $\pi^- + C$ interactions at 158 GeV/c with predictions of hadronic interaction models used in air shower simulations.

4.3.2 Cross section of $C+p \rightarrow B + X$ at 13A GeV/c (CR-G)

Recent progress in the detection of Galactic cosmic rays with space-based detectors such as PAMELA and AMS has led to a wealth of new data on the fluxes of leptons, nuclei and antiprotons from GeV to TeV energies with an unprecedented percent-level precision. These new data sets provide a unique diagnostic of cosmic-ray propagation in the Galaxy and an opportunity to find signatures of astrophysical dark matter annihilation. The amount of particle production in the Galaxy depends on the integrated traversed matter density which can be inferred from the ratio of secondary to primary cosmic rays such as the ratio of Boron to Carbon if the nuclear fragmentation cross section of the primary particles are known from laboratory measurements. The current uncertainties in the modeling of the propagation of cosmic rays in the Galaxy due to uncertainties of these cross sections is however at the level of 10–20% [61–64] and thus much larger than the uncertainty of the cosmic-ray data itself.

To remedy this situation, the NA61/SHINE Collaboration is studying the possibility of performing new precise measurements of nuclear fragmentation at the CERN SPS. A pilot run [65] took place in December 2018 and recorded 3 days of test data for the measurement of Boron production in C+p interactions.

For this purpose, the SPS delivered secondary ions to the NA61/SHINE experiment that were created by fragmenting a primary lead beam on a primary beryllium target (see [66] for a description of previous data taking of NA61/SHINE with a secondary ion beam). A measurement of the resulting beam composition at the experiment is shown in Fig. 25 for two different beam rigidities $R = E/Z$ and primary target thicknesses. As can be seen, even for the uncalibrated online data shown here, the beam isotopes are well separated by measuring their time of flight with two scintillators separated by 236 m and the amplitude of the scintillator signals which is proportional to the squared charge of the particle. The settings on the right panel were used for the fragmentation run presented here as it maximized

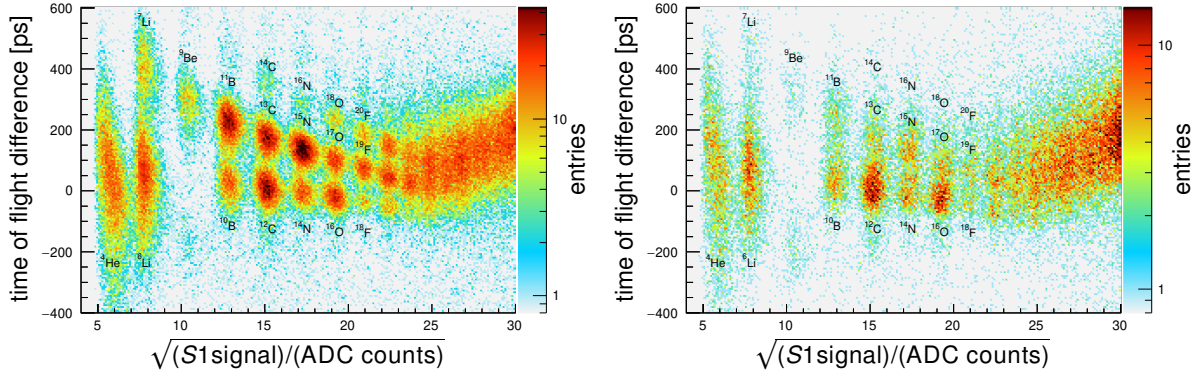


Figure 25: Beam composition recorded with free-running trigger detectors for different settings of the H2 beamline. Left: $E/Z = 28$ GV, 20 cm primary Be target, right: $E/Z = 27$ GV, 16 cm primary Be target. The signal on the x-axis is proportional to the charge of the beam particle, whereas the y-axis separates the isotopes masses via a measurement of the particle velocity.

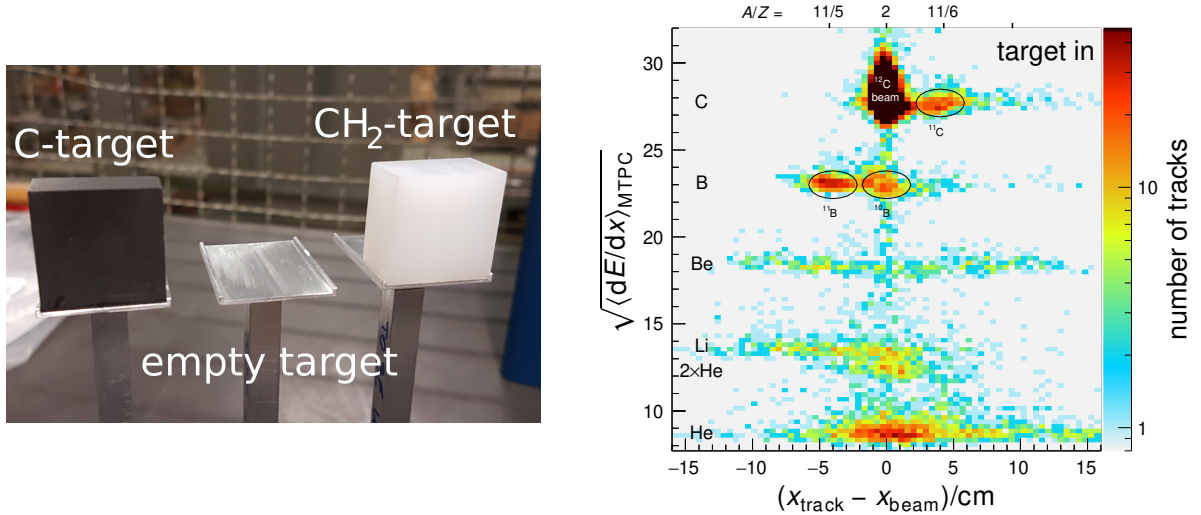


Figure 26: Left: targets used for the data taking, right: detection of fragments in the TPC downstream of the magnetic field (see text)

the number of ^{12}C ions in the beamline. The main beam trigger was set to select carbon isotopes.

More than 1.1×10^6 carbon beam triggers were recorded during three days of data taking sliding into the beam three alternative targets as indicated on the left panel of Fig. 26: A 1 cm C-target, a 1.5 cm polyethylene (CH_2) target and an empty target holder. The latter is used to correct the measurement for out-of-target interactions and the subtraction of C+C interactions from C+ CH_2 interactions yields the desired fragmentation cross sections in C+p interactions (details of the analysis can be found in [67]).

The identification of fragments downstream of the target is illustrated in the right panel of Fig. 26. Here the x-axis shows the deviation of the measured track from the nominal beam position after the passage through the two superconducting magnets. This deviation is a measure of the rigidity of the particle relative to the beam rigidity and thus of the mass of

the produced isotope. On the y-axis, the square root of the energy deposit in the TPC is plotted, which gives a measure of the charge of the particle. Since the data were taken in zero-bias mode, most tracks are in the ^{12}C -peak appearing as a black area in the truncated color scale. ^{11}C , ^{11}B and ^{10}B fragments are clearly visible and also Be and Li fragments, though the statistics of the pilot run is too small to discern the different isotopes of the latter by eye.

As a first step, the analysis concentrated on the sum of B isotopes. The fully calibrated Z^2 distribution derived from the energy deposit in the TPC located 10 m downstream of the target is shown in Fig. 27. As can be seen, the different charges are well separated with almost no overlap between the elements. The gray histogram shows the distribution of charges without inserted target, i.e. isotopes that were produced in interactions with the detector material. The data points correspond to the charge distribution with inserted target and the red arrows indicate the range in Z^2 used to select B nuclei.

The number of B nuclei produced in C+C and C+CH₂ interactions was used to derive a preliminary measurement of the fragmentation cross section of C on p to B [68]:

$$\sigma_{\text{C+p}\rightarrow\text{B+X}} = (47.7 \pm 3 \text{ (stat.)} \pm 2.3 \text{ (syst.)}) \text{ mb.}$$

This measurement is compared to previous data in Fig. 28 and agrees well with the extrapolation of the cross section derived in Ref. [64] and indicated by the shaded bands. It is worthwhile noting that the asymptotic value of the cross section above 10 A GeV/c is very important for the interpretation of the B/C ratio measured by AMS up to $\gtrsim\text{TeV}$ [69]. In this energy range only one measurement from Ref. [70] was available prior to the NA61/SHINE pilot run.

As detailed in Ref. [71], a whole range of nuclear reactions needs to be measured to allow for a precise measurement of light secondary nuclei in cosmic rays. The variety of secondary fragments delivered by the H2 beamline (cf. Fig. 25) is ideal for collecting this data at the SPS with a single beam setting in a short time. Such a measurement campaign is proposed to

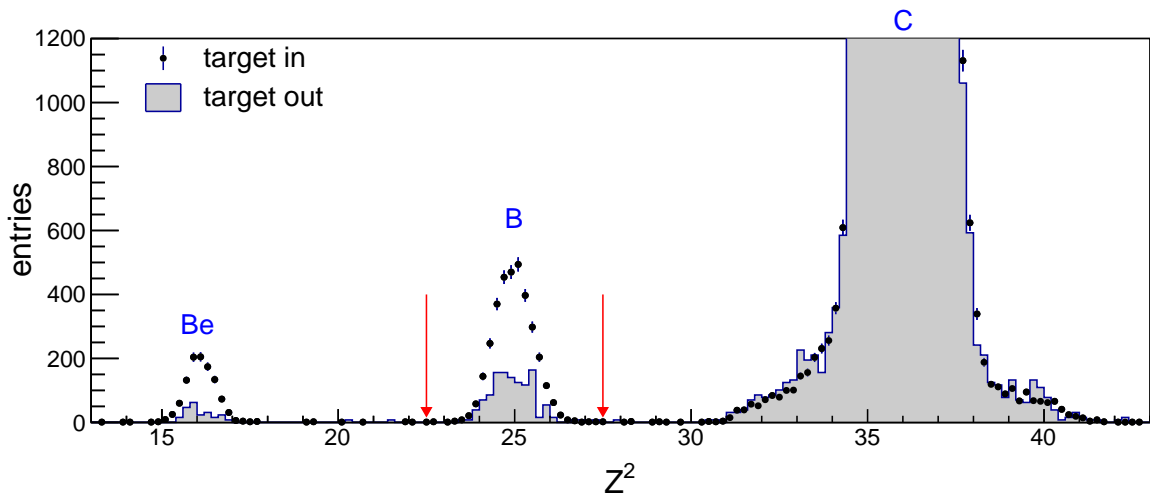


Figure 27: Distribution of the squared track charge measured with the TPC located about 10 m downstream of the target (see text).

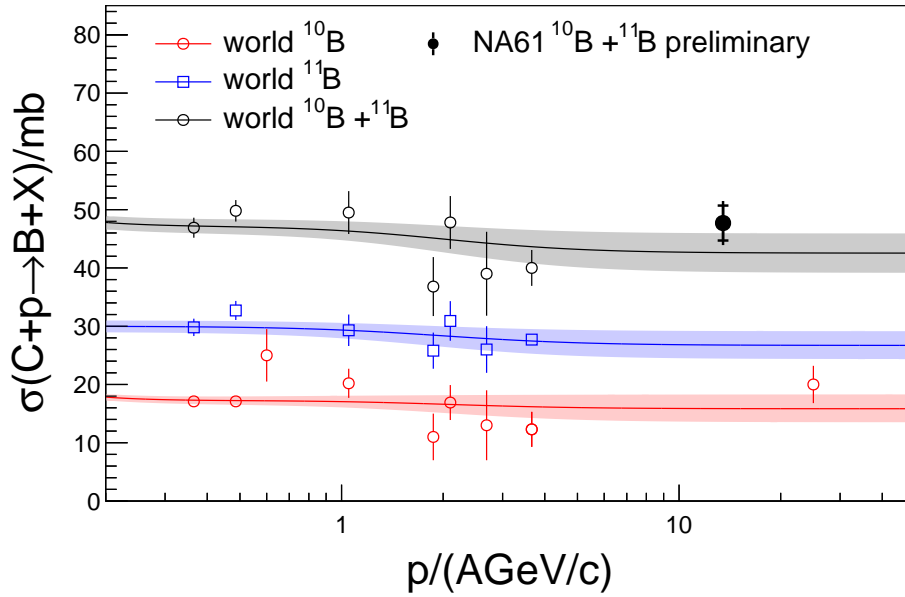


Figure 28: Measured fragmentation cross section of $C + p \rightarrow B + X$ (filled data point) compared to previous measurements (open data points) and the parameterization of the fragmentation cross section from (see [64] and references therein).

take place when the LHC (and thus SPS) resume operation after the current “long shutdown 2” [72]. The envisaged data taking will benefit from the planned upgrade of the read-out system of NA61/SHINE to increase the possible data taking rate by a factor of ten, bringing it up to 1 kHz. At this readout speed a modest beam time of about two weeks of data taking with secondary ions from the SPS would lead to a comprehensive measurement of the most relevant cross sections for the secondary production of the cosmic-ray isotopes of Li, Be, B, C and N.

4.3.3 Analysis of \bar{p} and d production in $p+p$ interactions at 158 GeV/c (CR-G)

The existence of dark matter is established on very different length scales from galaxies to galaxy clusters to the cosmic microwave background [73]. Little is known about dark matter particles except that they are gravitationally interacting, but other than that only very weakly interacting - if at all - with regular matter.

Anti-deuterons may also be generated in dark matter annihilations or decays, offering a potential breakthrough in unexplored phase space for dark matter. The unique strength of searching for low-energy anti-deuterons lies in the ultra-low astrophysical background [74–79]. Low-energy anti-deuterons from a wide range of viable dark matter models [76, 77, 80] exceed the astrophysical background [81] by $\mathcal{O}(100)$ below a few GeV/nucleon. This is in strong contrast to positrons, anti-protons, and γ rays where only a small contribution on top of the background is expected in optimistic scenarios.

Anti-deuteron Formation

Although the predicted low-energy flux of antideuterons from dark matter annihilations or decays is much higher in many models, the uncertainties of anti-deuteron formation and propagation are on the order of a factor of 10 and should be reduced for a more powerful dark matter interpretation. The formation of nuclei in hadronic interactions is described by different models. It is an important question whether (anti-)deuterons are produced at chemical freeze-out from a quark-gluon plasma or at a later stage via coalescence. The conclusion of the following short overview is that more experimental data and better modelling of (anti-)deuteron formation are needed.

Coalescence Model

The fusion of an anti-proton and an anti-neutron into an anti-deuteron can be described by the simple coalescence model, which is based on the assumption that any pair of (anti-)proton and (anti-)neutron within a sphere of radius p_0 in momentum space will coalesce to produce an (anti-)nucleus. The coalescence momentum p_0 is a phenomenological quantity and cannot be calculated from first principles. Therefore, it has to be determined through fits to experimental data [82]. In this approach, the (anti-)deuteron spectrum is given by:

$$\gamma_d \frac{d^3 N_d}{dp_d^3} = \frac{\pi}{6} p_0^3 \left(\gamma_p \frac{d^3 N_p}{dp_p^3} \right) \left(\gamma_n \frac{d^3 N_n}{dp_n^3} \right), \quad (3)$$

where p_i and dN_i/dp_i are, respectively, the momentum and the differential yield per event of particle i (d =(anti-)deuteron, p =(anti-)proton, n =(anti-)neutron). The coalescence momentum is a critical value because it enters to the third power and directly scales the yield, and as such the cosmic-ray flux. The state-of-the-art technique is to apply the coalescence condition to $\bar{p} \bar{n}$ pairs on a per-event basis in Monte Carlo simulations. Tuning to experimental data typically yields best-fit p_0 values in the range of about 100 MeV/ c , which is smaller than the typical scale at which the perturbative theory of Quantum Chromodynamics breaks down. As a result, the coalescence model is sensitive to non-perturbative effects in the hadronic generators. p_0 heavily depends on the hadronization model because it also describes all other differences between antiproton and antideuteron production.

A recent study [83] combined results from existing anti-deuteron measurements. The left panel of Fig. 29 illustrates the best current understanding of the coalescence momentum p_0 Eq. (3) for anti-deuteron production as a function of energy in the laboratory frame. The underlying data sets come from many different experiments, some dating back several decades. The different points are derived from mostly poorly constrained production cross section spectra. Due to the shape of the primary cosmic-ray spectrum, especially interesting for the understanding of cosmic-ray anti-deuterons is the steep increase of the coalescence momentum between 10 to 100 GeV/ c of beam momentum.

Thermal model

The production of light nuclei in $p+p$ interactions can also be discussed in a thermal model approach, where the hadronization happens in fireballs [85–87]. The resulting particle spectra can be used to examine the conditions at freeze-out. In this model, the particle yields depend approximately exponentially on the chemical freeze-out temperature T_{chem} and the mass m : $dN/dy \propto \exp(-m/T_{\text{chem}})$. Due to their large masses, the abundance of nuclei is

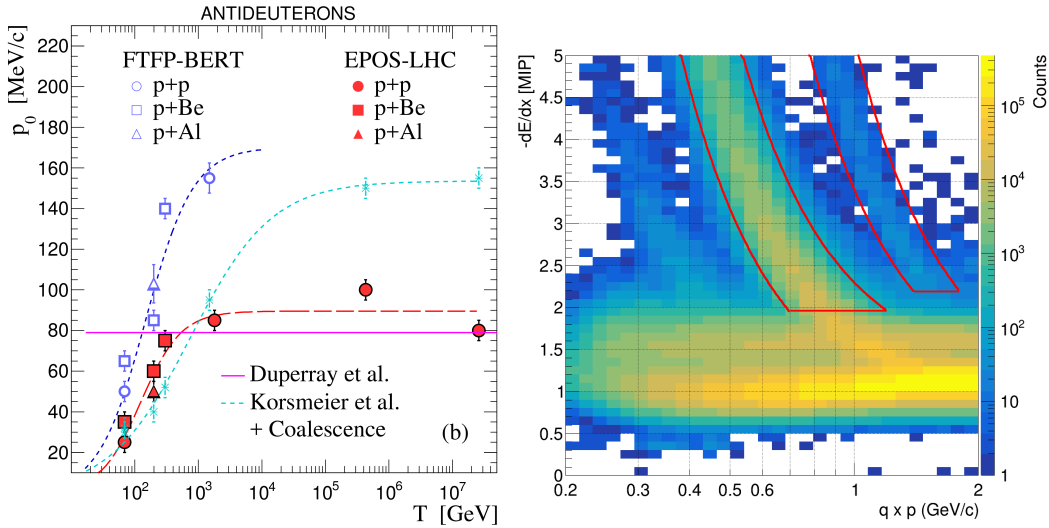


Figure 29: *Left:* Coalescence momentum p_0 (see Ref. [83]) for anti-deuterons as function of collision kinetic energy (T) for two different hadronic generators. Fits for EPOS-LHC (long-dashed red line) and FTFF-BERT (dashed blue line) are shown. Additionally, the p_0 values obtained from the analytic coalescence model and the parametrization of Korsmeier et al. are included. [84] The Geant4 FTFF-BERT model could not be used to simulate the highest energies. *Right:* Distribution of charged particles in the $dE/dx - p_{lab}$ plane. The energy loss is measured in the TPCs, and is shown for charged particles for events and tracks selected for the analysis of p+p interactions at 158 GeV/c. The selection region for low-momentum protons and deuterons is highlighted, and is calculated based on the Bethe-Bloch function.

very sensitive to T_{chem} . The value of T_{chem} obtained from data is about 170 MeV and shows a weak energy dependence.

Production of secondary deuterons The p+p 158 GeV/c data sets from 2010 and 2011 containing about 60 million events were analyzed, and about 1000 low-momentum deuterons were identified. However in the most common channels for deuteron production in p+p collisions (eg $p+p \rightarrow d+\bar{n}+p$ and the resonance production channel $p+p \rightarrow d+\pi^+$), it is kinematically infeasible to produce deuterons with p_{lab} less than about 1.4 GeV/c when the beam momentum is 158 GeV/c. The right panel of Fig. 29 shows the selected deuterons tracks which have passed the event and track selection cuts in the analysis. Using Monte-Carlo simulations of detector acceptance and efficiency, the correction factor for protons was determined to be about ten in this kinematic region. Assuming a similar correction factor for deuterons, an estimated 10,000 deuterons should be produced in this kinematic region. The source of these low-momentum deuterons was investigated. The left and right panel of Fig. 30 show the background-corrected vertex-Z distribution of selected events containing at least one proton and at least one deuteron, respectively. The plots show no excess of proton or deuterons from regions close to the target-holder. Hence, the target holder was not the source of these deuterons.

Deuteron production from the interaction of secondary protons (produced in the primary p+p interaction) with the target medium was investigated. The deuteron resonance production cross-sections were obtained from other experiments having low beam momentum p+p collisions (see Ref. [83]). EPOS simulations were used to get the secondary proton spectra for p+p 158 GeV/c. The p-p interaction cross-sections for various secondary proton momenta

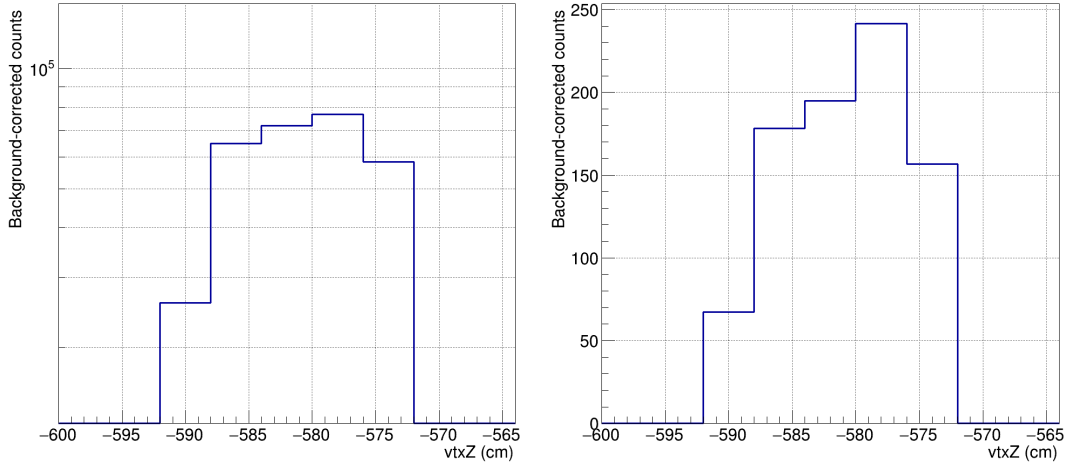


Figure 30: The distribution of the z -coordinate of the vertices of selected events containing at least one proton (left), and at least one deuteron (right).

were obtained from PDG. The secondary proton was assumed to be produced on average in the middle of the target, hence its interaction probability was set to half of the interaction probability of a beam proton of same momentum. Using these, it was estimated that 2500 deuterons (i.e a quarter of the deuteron signal) are produced via this process. The remaining signal could have been produced by interactions of the beam with residual gas in the beam pipe or by secondary interactions in detector material and which were mis-reconstructed to originate from within the target region.

Path Onwards Template fitting of dE/dx distributions is currently ongoing. Further momentum range widening will be achieved by using time-of-flight (*tof*) information. This will be particularly critical to measure deuteron spectra in the 5-10 GeV/ c momentum region. Measuring charge, momentum, and velocity, mass reconstruction in NA61/SHINE is possible up to a maximum momentum of about 10 GeV/ c (restricted by timing resolution), which corresponds to the momentum range accessible for deuterons by the cosmic-ray experiment AMS-02.

The \bar{p}/p ratio as a function of transverse momentum will be determined from the dE/dx analysis. Furthermore, the d/p ratio as a function of transverse momentum will be determined from the *tof* analysis. This will be used to tune hadronic generators as well as to test the coalescence and thermal model approach. The analysis of ALICE data [88] suggests that the thermal model works well for Pb+Pb interactions, but that the d/p ratio is over-predicted for p+p interactions. As it is more relevant to cosmic rays, this finding will be tested at the lower SPS energies.

The underlying mechanisms of hadronic generators are very different and it cannot be expected that two-particle correlation models agree. There is also no a-priori reason to expect the two-particle correlations from one generator to be more reliable than from another. Therefore, an important study is to compare angular correlations between (anti-)protons and (anti-)neutrons for different generators. For this purpose the differences in azimuthal angle $\Delta\phi$ and in pseudo-rapidity $\Delta\eta$ of nucleon pairs will be investigated. Like many fixed-target

experiments, NA61/SHINE does not have experimental access to (anti-)neutron spectra. Therefore, only pp , $p\bar{p}$, and $\bar{p}\bar{p}$ correlations can be studied experimentally and compared to simulations. This is a crucial step for validating and/or tuning the underlying hadronic models.

5 Detector upgrade

NA61/SHINE proposed [72] to continue the measurements of hadron and nuclear fragment production properties in reactions induced by hadron and ion beams after the Long Shutdown 2. The measurements are requested by heavy ion, cosmic ray and neutrino communities and they will include:

- (i) measurements of charm hadron production in Pb+Pb collisions for heavy ion physics,
- (ii) measurements of nuclear fragmentation cross section for cosmic ray physics,
- (iii) measurements of hadron production induced by proton and kaon beams for neutrino physics.

NA61/SHINE is the only experiment which will conduct such measurements in the near future.

The new measurements require upgrades of the NA61/SHINE detector that shall increase the data taking rate to about 1 kHz. These are:

- (i) Construction of a new Vertex Detector.
- (ii) Replacement of the TPC read-out electronics.
- (iii) Construction of a new trigger and data acquisition system.
- (iv) Upgrade of the Projectile Spectator Detector.
- (v) Construction of new Time-of-Flight detectors.

Also a feasibility study was requested of very low momenta (1-5 GeV/c) hadron beams needed for data taking for J-PARC and FNAL neutrino experiments.

The status of the detector upgrade and its funding is presented in this section.

5.1 TPC Upgrade

This section describes status and plans of the TPC upgrade. In the upgrade planning for the NA61/SHINE experiment described in Ref. [72] a list of work packages was defined for the upgrade of the TPC. Here the progress of the upgrade is presented following this list.

Status of the work packages for the upgrade of the TPC readout

(i) Development of a 3-D model of the NA61/SHINE readout chambers:

This work is finished and only final details for the mounting of the FECs and the cooling plates need to be considered and are described later.

(ii) Development, construction and tests of prototype input adapter cables:

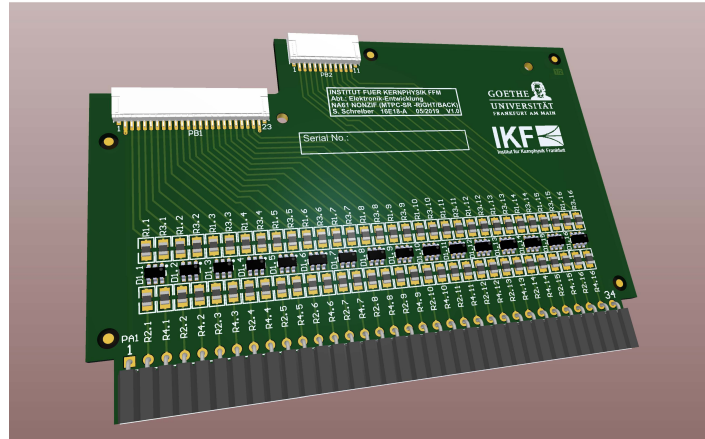


Figure 31: New design of the input adapter board with protection circuitry and two connectors on the output side for the Kapton cables connecting to the FEC.

Based on the 3-D model prototype adapter boards including an ESD protection network were developed and built in Frankfurt using the rigid/flex technology to incorporate the Kapton cables, see [72]. The very first test of the effect of the protection network and the increased length of the adapter cables on the noise performance of the FECs was tested in an existing test stand at IKF. The results are described below.

In the on-detector test it was found that the original idea to use the rigid/flex technology for the design of the input adapter boards together with the Kapton cables connecting to the FECs did not work properly. The weight of the 4 Kapton cables together with the input board made the handling rather tricky and lead to bent pins on the chamber connector side due to uneven forces when inserting the adapter boards. Therefore it was decided to go back to conventional technology and separate the Kapton cables from the adapter board. The new design, now with two output connectors, is shown in Fig. 31. Tests are foreseen within the next month.

(iii) Design of the mechanical support of the FECs:

Using the 3-D model a mounting scheme for the VTPCs was developed. Due to the limited space above the chambers given by the presence of the magnets the FECs have to be mounted in an inclined pattern shown in Fig. 32. In addition the readout adapter boards who's original layout was developed by the PHOS detector in Alice had to be redesigned to minimize space requirements. In particular the copper pipes of the cooling plates had to be taken into account requiring a shift of the board position towards the center of the FEC (see v)

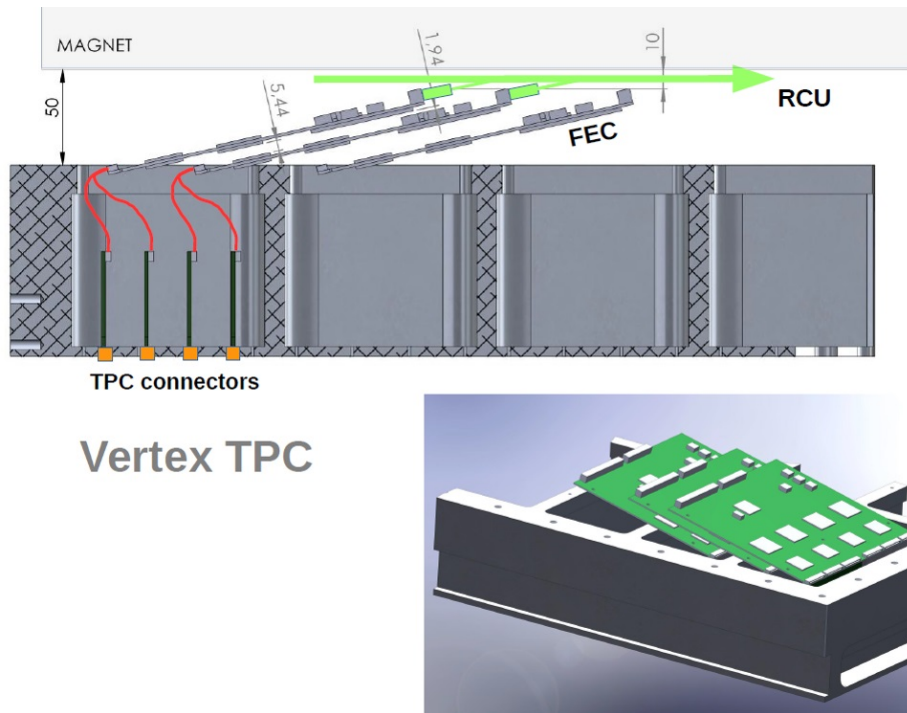


Figure 32: Simulation of FECs in a VTPC (not showing the cooling plates).

Due to the tight space it is necessary to use the original Alice cooling plates visible in Fig. 33 in a real VTPC chamber.

For the MTPCs the situation is much more relaxed as sufficient space is available.

In Fig. 34 a design study is shown where the FECs are sandwiched between the old NA61/SHINE cooling plates.

(iv) **Design and implementation of the FEC cooling:**

The FECs will be cooled following the present NA61/SHINE scheme and even use the existing cooling plates. Another option is the use of fans to remove the heat. This will be decided once the mounting schemes have been developed and the space constraints are better known.

(v) **Production and tests of interface boards for the connection of the FEC output to the flexible buses:**

First tests of the readout of the FECs using the RCU2 board within NA61/SHINE were done using interface boards developed for the PHOS detector in ALICE using the same FECs and RCUs as the TPC. This was done in the lab at Bergen. After the correct operation was established the same set-up was used for the on-detector test using two FECs described below. During these tests it was found that the two interface boards were so closely spaced (see [72]) that it was difficult to operate the locks. In addition it was realized that one side of the larger adapter board would interfere with the cooling pipe of the FECs planned to be used in the VTPCs. Therefore a redesign of the adapter boards was attempted combining the 2 separate boards into one and at the same time shift the



Figure 33: FECs in a VTPC showing the cooling plates.

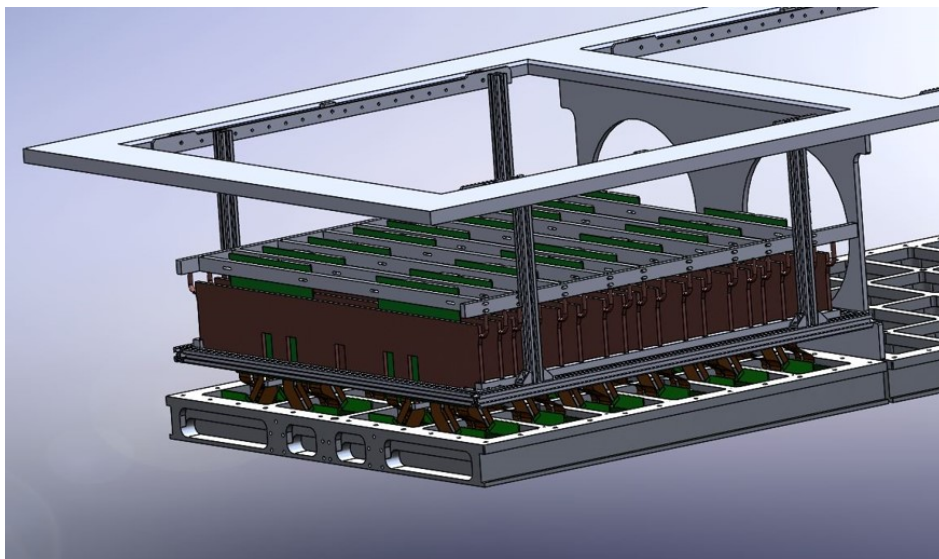


Figure 34: Model of the mounting of FECs in a MTPC together with the old NA61/SHINE the cooling plates.

position of the adapter board towards the center of the FEC to allow the passage of the cooling pipe.

The result is shown in Fig. 35. First tests using the new board will be performed within the next month.

- (vi) **Development of read-out and DAQ for the new electronics:** A rudimentary readout scheme for the RCU2 was developed for the on-detector tests described below. Work

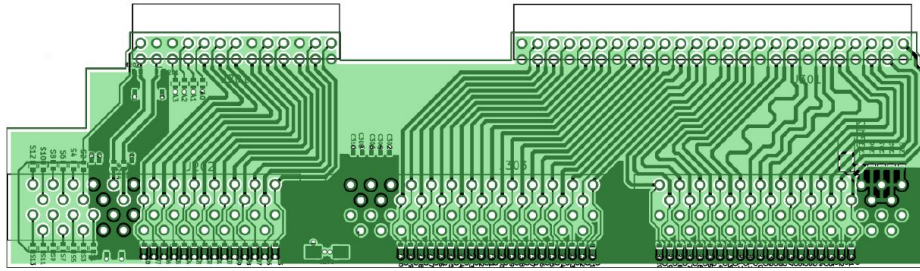


Figure 35: New design of the readout adapter board to connect a FEC to the three flexible readout bus cables.

for the final readout of the full TPC is ongoing.

- (vii) **Laboratory tests of the new readout chain:** Tests of the readout of several FECs in the lab using the full read-out chain (FECs, flexible cables, small adapter boards, RCU2s) have been performed at Bergen, at CERN and Warsaw University of Technology.

These tests culminated in an on-detector test with beam using two FECs and one RCU2 with a simplified readout scheme. The results are described below.

- (viii) **Design and implementation of a new Low Voltage system:** The new readout system requires power supplies, bus bars and cables for the distribution of the low voltage (LV). A first layout has been developed optimising the number of FECs connected to a given power supply.

It follows the design of the ALICE TPC LV system using power supplies from the company Wiener. For the distribution of the LV inside the MTPCs a group of 5 chambers is supplied by 5 bus bars running along the inside of the top plate on the side of the chambers perpendicular to the beam direction. For the VTPCs 3 chambers in beam direction are supplied by one bus bar running along the outside (away from the beam) of the VTPCs. The full layout is sketched in Fig. 36.

The connection between bus bars and FECs is then done by short patch cables as in Alice.

As an alternative to the relatively expensive power supplies from the company Wiener a development of new power supplies based on standard industry modules has been started in Krakow. If successful it will be used instead of the Wiener PS which remain the plan B option.

- (ix) **Development and implementation of new Detector Control System (DCS):** Work ongoing see subsection "DCS upgrade".
- (x) **Dismounting electronics from Alice and mounting in NA61/SHINE:** The first part of this work package is done: 1000 FECs with cooling plates for the VTPCs, 1000 FECs without cooling plates for the MTPCs and 100 RCUs were dismounted and transported to and stored in the NA61/SHINE experimental area.

The re-installation in NA61/SHINE of the the FECs will be done in due time.

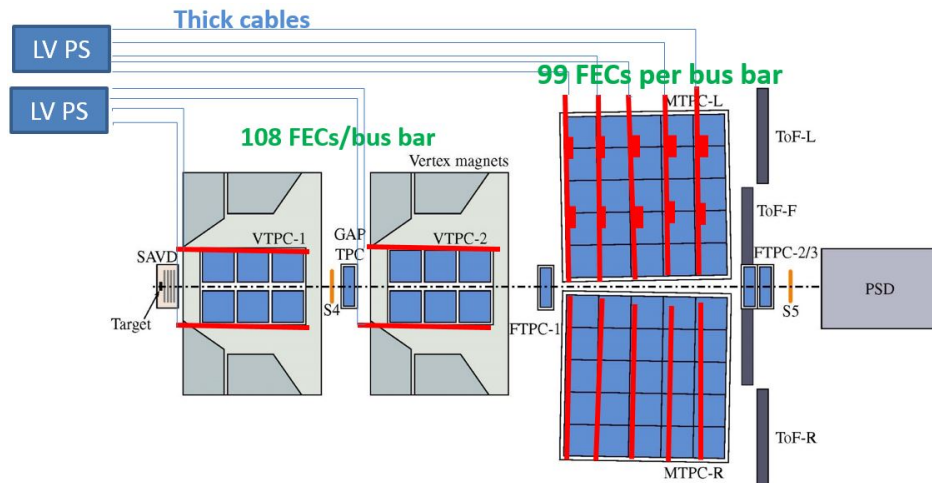


Figure 36: Positions of the bus bars (in red) on the VTPs and MTPCs. For MTPC-R not all details are shown.

5.1.1 First test results

During the last running period of NA61/SHINE in 2018 the first test results were obtained for work packages 2 and 5.

In a first step the additional noise of the new input adapter boards was determined using the same lab test stand that had been used in Alice to do the acceptance tests for all FECs. It was found that the increase of noise of the new about 13 cm long Kapton cables together with the additional ESD protection (100 Ω resistors and NUP suppressor diodes) is about 14% higher compared to the old Alice cables with 7 cm length.

In a special test run two Alice FECs were mounted in a high resolution sector of one of the MTPCs. On the input side prototypes of the new input adapter cables were installed while on the output side prototypes of the new cable readout bus with the corresponding adapter boards and one RCU2 interface board was used. In Fig. 37 left a comparison of the signal-to-noise ratios of the present NA61/SHINE electronics to the Alice FECs is shown. Clearly the new board fulfills the requirements.

5.2 TDAQ Upgrade

A new design of the Trigger and Data AcQuisition system (TDAQ) has been prepared along with the NA61/SHINE upgrade plan [72]. It is depicted in Fig. 38

The Detector Layer is the starting point of data flow. The technology used to transport data between those layers as well as everything inside the Detector Layer are not part of the TDAQ project. Thus sub-detector groups can freely choose the technologies for data collection and transport. Details are provided in sections dedicated to the corresponding sub-detector.

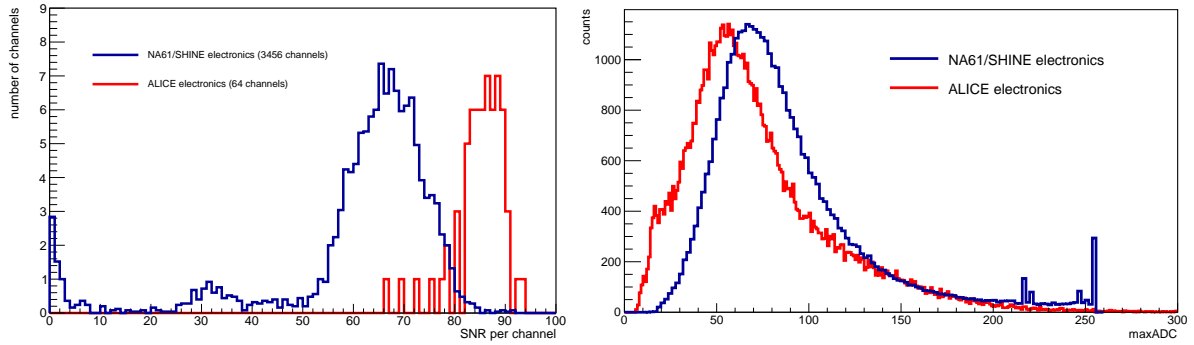


Figure 37: *Left:* Signal-to-noise of the NA61/SHINE legacy electronics compared to the new Alice readout. *Right:* Maximum signal of the track clusters of the NA61/SHINE legacy electronics compared to the new Alice readout.

The Readout Layer consists of nodes, which are sub-event builders. Components acquired up to now: about 300 machines to serve as Event Builders and Nodes; 12 units of 1GbE network switches for control and part of the data networks; one switch network which will be evaluated as TDAQ data network core switch. Furthermore, work on the communication library is well advanced.

The Acquisition Supervisor is an integral and central part of the DAQ system and, at the same time, the most crucial one. Already dedicated hardware has been obtained for the TDAQ Acquisition Supervisor. Currently, software development is in progress.

The Event Builders receive sub-events from all nodes and assemble a final event. Recently, a testbed was prepared using hardware dedicated for the final TDAQ setup. It is used for ongoing work on the software for Event Builders. Significant progress has already been made implementing data reduction methods such as local tracking and noise detection.

The Storage will be provided by CERN in form of CASTOR and EOS, where NA61/SHINE has already reserved 5 PB and 1 PB of storage space, respectively. Furthermore a data buffer will be installed, to cope with possible interruptions of the network connection to EOS. A second-hand disk array storage with the required capacity was already received. If funds are sufficient, a brand new storage system will be purchased. Furthermore, two 100 GbE connections are prepared and will be installed with the help of the CERN IT department in 2020.

During LS2 the NA61/SHINE trigger system will undergo a major upgrade. The old system based on CAMAC components (main logic unit, pattern units, scalers etc.) will be replaced by a new system based on modern VME parts. The core of the new trigger system will be a CAEN V2495 programmable logic unit based on FPGA. Custom firmware for the CAEN module will be developed for this purpose, which will handle the trigger logic required for efficient operation of the NA61/SHINE detector system. Moreover, the new trigger system will incorporate BUSY logic of the data acquisition programmed in FPGA fabric. A custom trigger distribution system will be introduced, together with control and monitoring software. Development of the new trigger system is well advanced, work on the custom FPGA firmware has already started. After LS2 NA61/SHINE will use legacy ALICE TPC electronics, which require a TTC (Timing Trigger Control) signal used by LHC experiments

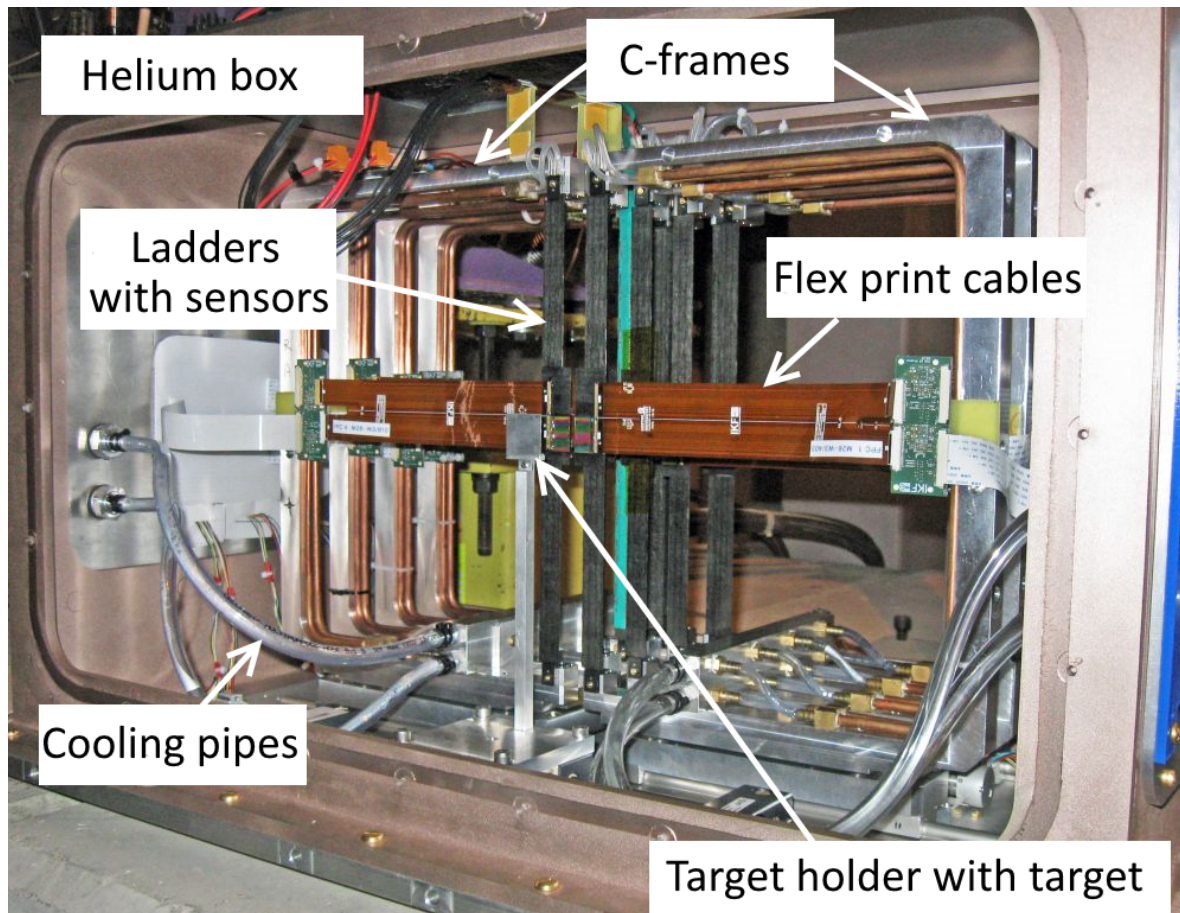


Figure 39: The SAVD used by NA61/SHINE during the data taking in 2016 and 2017

5.3 VD Upgrade

The upgrade of the existing SAVD detector aims to adapt this detector to the requirements of data taking with a 1 kHz trigger rate, and to increase its geometrical acceptance. Both measures will yield a significant ($\sim 30\times$) increase of statistics of the reconstructed decays of charm hadrons.

To fulfill its task, the new Vertex Detector (VD) will have to provide a rate capability, which exceeds the one of the SAVD by one order of magnitude. The related data rate is found to surpass the possibilities of the successful MIMOSA-26AHR sensors used so far in the SAVD. Moreover, the related increase of the radiation dose has to be considered. The requirements on the sensors can be estimated by scaling the corresponding numbers derived for the SAVD [89] to the future running scenario. This is done assuming that the VD will operate at a true collision rate of 5 kHz, and at a duty cycle of 0.15. The results for the most exposed point of the VD and an operation time of 40 days are shown in Table 2. No safety margin was considered. One finds the radiation load dominated by the damage caused by direct beam ions from the beam halo, which varies substantially depending on the quality of the beam tuning. The table provides two numbers based on the scaling of initial assumptions as described in Ref. [89] and based on a measurement of the beam halo carried out during

Radiation source	Ionizing [krad]	Non-ionizing [$10^{12} n_{eq}/cm^2$]
Direct particles	35	1.3
Delta electrons	40	Negligible
Beam halo (scaled)	1200	2.0
Beam halo (measured)	200	0.3
Sum requirements	275-1275	3.3
ALPIDE	> 500	17.0

Table 2: Radiation doses for the most exposed point of the VD and a run of 40 days with 150A GeV/c Pb+Pb. For the radiation dose generated by the beam halo, numbers scaled from Ref. [89] (scaled) and numbers relying on measurements of the beam halo performed during the 2017 Xe+La run at 150A GeV/c (measured) are shown. The beam halo of the Xe-beam was reduced by means of careful beam tuning. The obtained numbers are considered as most representative for future experiments.

the 2017 Xe+La run at 150A GeV/c. One observes that optimizing the beam for a low beam halo yielded a significant reduction of the radiation load. Despite remaining moderate, the ionizing radiation dose still exceeds the radiation tolerance of the previously used MIMOSA-26AHR sensors.

The new detector will reuse the mechanics and infrastructure of the SAVD. A photograph of the SAVD just before its installation on the beam for the test measurement in 2016 is shown in Fig. 39. One can see vertically oriented carbon fibre ladders with MIMOSA-26 sensors installed in their centres as well as the Pb target of 1 mm thickness located about 50 mm upstream from the first SAVD station. The carbon fiber ladders are exactly the same as those used in the Inner Barrel of the new ALICE Inner Tracking System (ITS); the group of the St. Petersburg State University involved in their development and construction is also member of NA61/SHINE. More details on the construction and performance of the SAVD are provided in Ref. [72] and sec. 4.3.

In spite of the good experience with the MIMOSA-26AHR sensors in the construction and operation of the SAVD, the VD cannot be built using these sensors: in order to cope with the 10-fold increase in beam intensity and interaction rate better time resolution (by a factor of 10) is required. The ALPIDE sensor and the detector concept developed for the new ALICE ITS were found to be the best candidate for the VD in 2022. In December 2016 one ITS Inner Barrel stave with 9 ALPIDE chips, the green vertical structure in Fig. 39, was successfully operated in NA61/SHINE during 5 days of the test with Pb+Pb collisions at 150A GeV/c. An agreement concerning further collaboration and technology transfer from ALICE ITS to NA61/SHINE was already negotiated.

In the spirit of the above considerations the upgraded Vertex Detector (VD) will rely on the carbon fibre support structures developed for the ALICE ITS. Instead of the older MIMOSA-26AHR, they will host the modern ALPIDE CMOS Pixel Sensors [90]. A comparison of the features of both sensors is given in Table 3.

The new sensors feature a time resolution of 10 μ s, which is by more than one order of magnitude faster than the average time between two collisions, and a powerful ~ 1 Gbps data

Table 3: Comparison of basic parameters of MIMOSA and ALPIDE sensors.

	MIMOSA-26AHR	ALPIDE
Sensor thickness (μm)	50	50
Spatial resolution (μm)	3.5	5
Dimensions (mm^2)	10.6×21.2	13.8×30
Power density (mW/cm^2)	250	40
Time resolution (μs)	115.2	10
Detection efficiency (%)	>99	>99
Dark hit occupancy	$\lesssim 10^{-4}$	$\lesssim 10^{-6}$

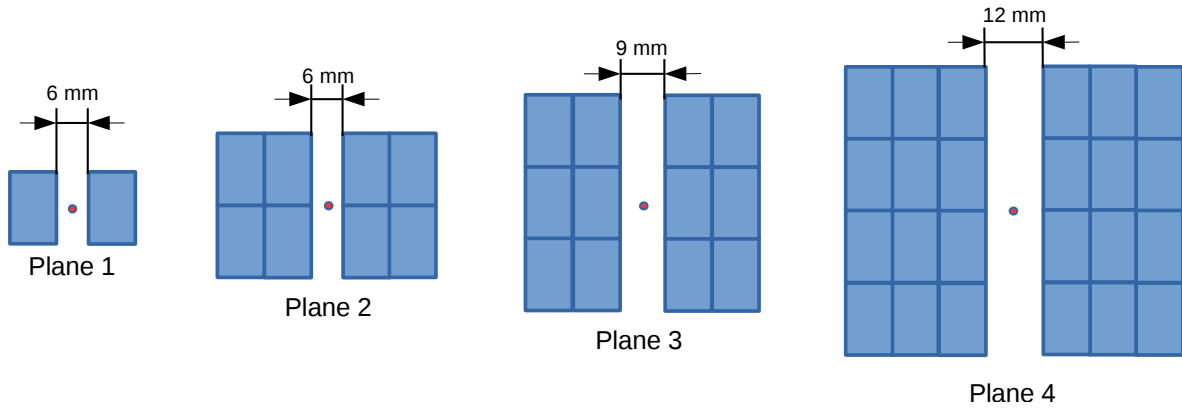


Figure 40: Schematic view of the VD layers based on ALPIDE sensors. From left to right: the first layer with two sensors, the second layer with 8 sensors, the third layer with 12 sensors and the fourth layer with 24 sensors. The total active area of the VD sensors is 190 cm^2 .

interface. This fact and the capability of ALPIDE sensors to use external trigger information for data reduction ensures the rate capability required for the VD. As shown in Table 2, the sensor does also match the requirements with respect to radiation dose. To estimate its tolerance to direct ion hits in terms of SEE, the sensor was operated for several days in a direct Xe-beam at the SPS in 2017 and no crucial incident was observed. This suggests that the chip is not particularly vulnerable and that no dedicated detector safety system for the case of beam displacement is required. Note that the tolerance of ALPIDE sensors to ionizing radiation likely exceeds the 500 krad guaranteed so far. This is a subject of ongoing research.

As the fibre supports were initially designed for ALPIDE sensors, the carbon fibre plates required for adapting them mechanically to MIMOSA-26AHR sensors become obsolete, which reduces the material budget by slightly below $0.1\% X_0$. Moreover, accounting for the very low power consumption of ALPIDE sensors, it is considered not to use the active cooling foreseen in the support structures. The absence of coolant in the structures would additionally reduce the material budget of the VD as compared to the SAVD. The obsolete front-end cards and readout electronics of the SAVD will be replaced as well.

Compared to the SAVD the new VD aims to increase the geometrical acceptance from 33% to

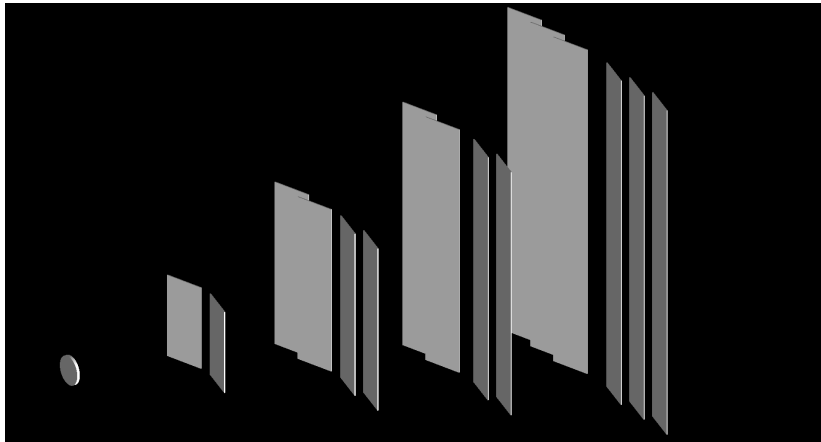


Figure 41: The GEANT4 visualisation of the VD detector geometry described in Fig. 40.

70% of the tracks also detected in the TPCs of NA61/SHINE. This number holds for a Pb+Pb collision system at $158A \text{ GeV}/c$. To reach this goal, it is planned to construct the detector from 16 ladders, which will hold 46 ALPIDE sensors with a total active surface of 190 cm^2 . The new sensor configuration is displayed in Fig. 40 and the related GEANT4 model used for the performance simulations is shown in Fig. 41. Note that the upgrade will require only minor modifications in the mechanical design, as the SAVD was already designed for compatibility with ALPIDE sensors and the related ladders.

5.4 DCS Upgrade

The absence of beam during the LS2 gives an opportunity to upgrade the Detector Control System.

Up to now, the system was based on the EPICS framework, which handled measurements and the exchange of information between different components. Unfortunately, the used version is slowly becoming outdated. The new, recommended version is very different from the previous one. Therefore, having in mind that the system is to be used for many years, it needs to be redesigned. This triggered a search for another framework that might better fulfill the requirements of NA61/SHINE.

The choice was made to use OPC UA [91] with its open source implementation open62541 [92]. OPC has been widely used across the industry and is becoming a standard in hardware communication.

Communication software of all currently used devices has been written as universally as possible, therefore migration does not require rewriting of all of the code. In fact, the process has already started as all the tests of the OPC itself had already finished. The communication part of the GUI still has to be rewritten.

Due to other upgrades, it became necessary to include newly installed devices in the DCS (e.g. new low voltage power supplies for the TPC readout electronics).

The upgrade will also include the DCS database. The current, relational PostgreSQL shall be replaced with a new, time-series database. Also, the java-based application to view the database contents will be replaced with its web-based equivalent.

5.5 PSD Upgrade

The Projectile Spectator Detector (PSD) is a segmented forward hadron calorimeter used by NA61/SHINE to determine the collision centrality and the orientation of the event plane. A precise characterization of the event class is of crucial importance for selection of event centrality at the trigger level as well as for the analysis of event-by-event fluctuation observables. The PSD is also important for improving the quality and kinematic range of measurements of collective flow in the collisions.

5.5.1 Performance of the PSD during the Pb+Pb data taking

In 2018 the PSD was used during the Pb-beam time. It served as the trigger detector for selecting central collisions. The energy reconstructed from the PSD measurements is shown in Fig. 42 (left) for different trigger types. The PSD energy is normalized to the beam energy. T1 is a beam trigger, T2 is an interaction trigger and T4 selects minimum bias interactions. Fig. 42 (right) shows the correlation between the number of reconstructed tracks and the energy in the PSD for the T2 trigger.

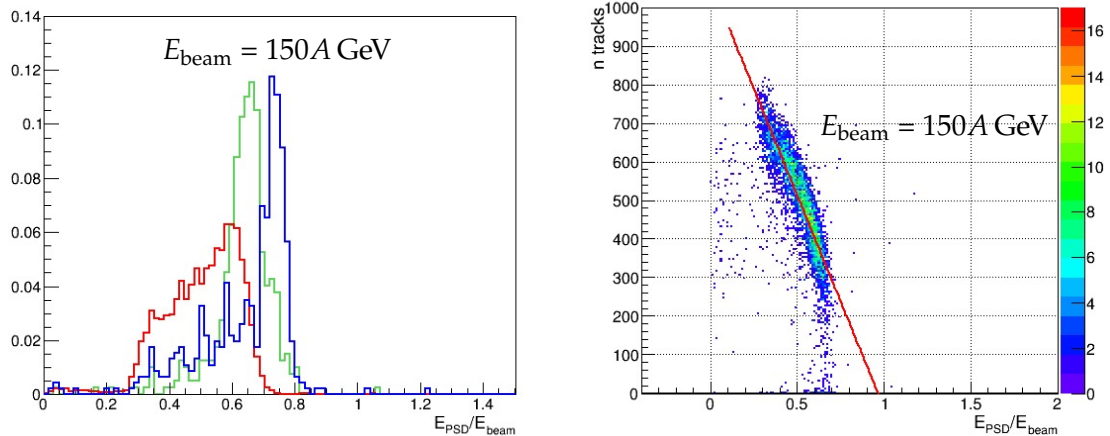


Figure 42: Performance of PSD during the 2018 Pb-beam period. *Left:* response of the PSD for different trigger types: T1 (green, beam trigger), T2 (red, interaction trigger) and T4 (blue, min.bias trigger). *Right:* correlation plot of number of tracks reconstructed versus the PSD energy.

5.5.2 PSD beyond 2020 upgrade

The NA61/SHINE physics program beyond 2020 requires an increase of the Pb-beam rate by more than one order of magnitude. This will lead to a high radiation level in the experimental area, because the present PSD is in effect an active beam dump. Therefore, the

PSD must be shielded by additional concrete blocks. This is practically impossible for the present calorimeter because it is placed on a movable platform with large transverse size which facilitates the required changes of the lateral PSD position during data taking.

To solve the above problems, it is proposed to use two calorimeters, a Main (M-PSD) and a Forward (F-PSD) Projectile Spectator Detector (see Fig. 43) instead of the present PSD. The M-PSD would be based on the present PSD with the 16 small central modules replaced by four new central modules with transverse sizes $20 \times 20 \text{ cm}^2$ and with truncated edges forming a beam hole of 60 mm diameter at the center. These modules were constructed for the calorimeter in the CBM (Condensed Baryonic Matter) experiment at FAIR (GSI). In addition, 8 cm thick boron polyethylene blocks placed at the rear side of each of CBM modules will reduce the neutron fluence incident on the readout MPPCs. The CBM and NA61/SHINE collaborations already signed an agreement for using the CBM calorimeter modules in NA61/SHINE.

The F-PSD is an additional small calorimeter placed at a distance of 4.6 m downstream of the M-PSD. It consists of 9 modules with transverse sizes of $20 \times 20 \text{ cm}^2$. All F-PSD modules will have $5.6 \lambda_{\text{int}}$ interaction lengths, the same as in the M-PSD. Scintillator plates of the central module of the F-PSD have holes in the center. This will reduce the radiation damage and prevent the scintillator from becoming dark and reducing the light yield. In order to avoid ageing effects in high radiation level conditions the CBM modules will be used only in the M-PSD and the F-PSD is constructed from old large PSD modules.

In 2019 the M-PSD has been rearranged. All 16 small modules were replaced with four $20 \times 20 \text{ cm}^2$ modules with truncated edges. A view of the installed M-PSD and F-PSD is shown in Fig. 44. Proposed shielding with concrete blocks is shown in Fig. 45. The next steps will be replacing the photodiodes of all modules with new Hamamatsu MPPCs. Large modules from the old PSD will be equipped with MPPCs S12572-015C/P ($15 \mu\text{m}$ pixel size) and new CBM modules with S12572-010C/P ($10 \mu\text{m}$ pixel size). This will balance signals from small light yields of the old modules and high light yield from the new ones.

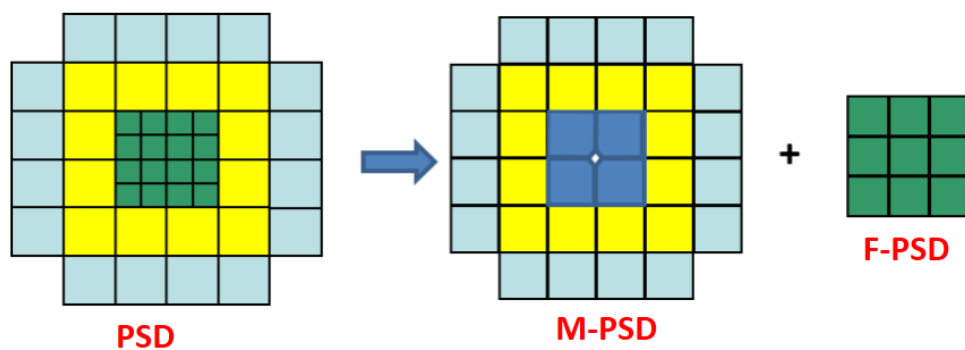


Figure 43: Schematic front view of the current PSD and the proposed new M-PSD and F-PSD calorimeters.



Figure 44: View of the modified M-PSD and F-PSD in the NA61/SHINE beam line.



Figure 45: Schematic view of F-PSD shielding.

5.6 MRPC Upgrade

The previous Time of Flight (ToF) identification system of NA61/SHINE consisted of two walls of 891 scintillation detectors each. The time resolution of the scintillator ToF walls was about 75 ps, allowing separation of kaons from pions up to a momentum of 8 GeV/c [93]. After 20 years of operation all parts of the system require upgrades due to significant ageing of scintillators, photo-multipliers, power supplies as well as the obsolete readout electronics and cables. New ToF detectors based on multi-gap resistive plate chambers (MRPC) were proposed as replacement [94]. The upgrade of ToF-LR is planned to be completely ready by 2022. The new time-of-flight detectors must provide performance similar to the present ToF-LR detectors in order to successfully perform the NA61/SHINE physics program [72]. Therefore, requirements for the new ToF system should be as follows:

- (i) high efficiency ($> 95\%$);
- (ii) excellent intrinsic time resolution (< 75 ps);

- (iii) high granularity in order to keep the overall system occupancy below 15%;
- (iv) good position resolution to provide effective matching of the ToF hits with the Time-Projection Chambers (TPCs) tracks;
- (v) low power dissipation in close proximity to the TPCs.

5.6.1 Design concept of the new ToF system

In order to achieve the required performance, two types of MRPCs were considered for the NA61/SHINE ToF wall:

- (i) "narrow" with 15 cm strip readout;
- (ii) "wide" with 30 cm strip readout.

The counters have fully differential, symmetric, triple-stack architecture [95]. Signals are read out at both strip ends. The advantage of the strip electrode for readout is the reduction of the number of channels making the system more cost-effective. Overall dimensions of the MRPC are $610 \times 330/180 \times 25 \text{ mm}^3$. The active area is $600 \times 300 \text{ mm}^2$ for the "wide" detectors or $600 \times 150 \text{ mm}^2$ for the "narrow" detectors, respectively. The scheme of the MRPC detector is presented in Fig. 46. The structure of the MRPC is described in detail in Ref. [72].

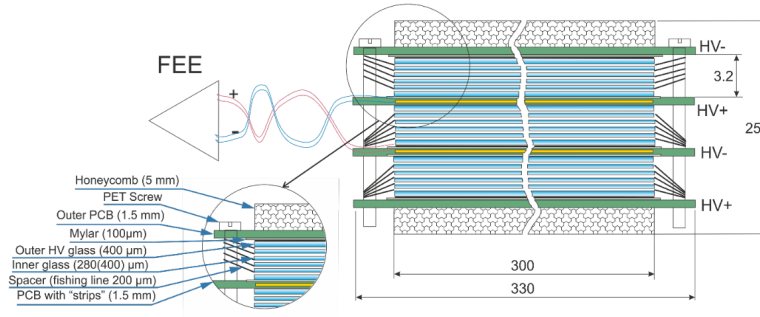


Figure 46: Scheme of the triple-stack MRPC with strip readout.

The mounting structure of the new NA61/SHINE ToF-LR will be composed of two symmetric modules – the gas tight boxes, which will be integrated into the frame that was used by the old ToF system. The modules containing the MRPCs will be made of aluminum structural channel and aluminum honeycomb. The total gas volume of a module is approximately 1 m^3 without taking into account the detectors. In order to keep the occupancy below 15%, each module will consist of two columns with "narrow" detectors and one with "wide" ones.

The MRPCs will be positioned inside the modules at an angle of 7.5° with the front honeycomb plate as shown in Fig. 47. The detector location inside the modules was designed to minimise losses of the sensitive area along the x and y axes. Adjacent detectors will be positioned on the column to create an overlap of about 30 mm between two adjacent MRPCs at the edge of the active area. The overlapping regions provided between two columns amounts to about 55 mm of active area. (Fig. 48). This will ensure minimum geometrical

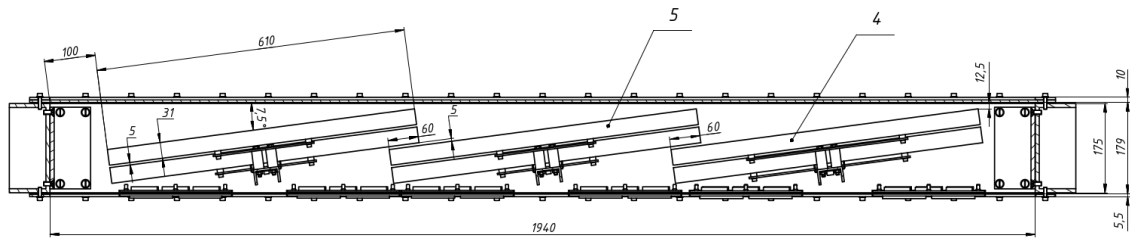


Figure 47: Top view of the TOF module. Position of the MRPCs correspond to the TOF-L position.

inefficiency and inter-calibration possibility of the detectors via tracks traversing two or more of them.

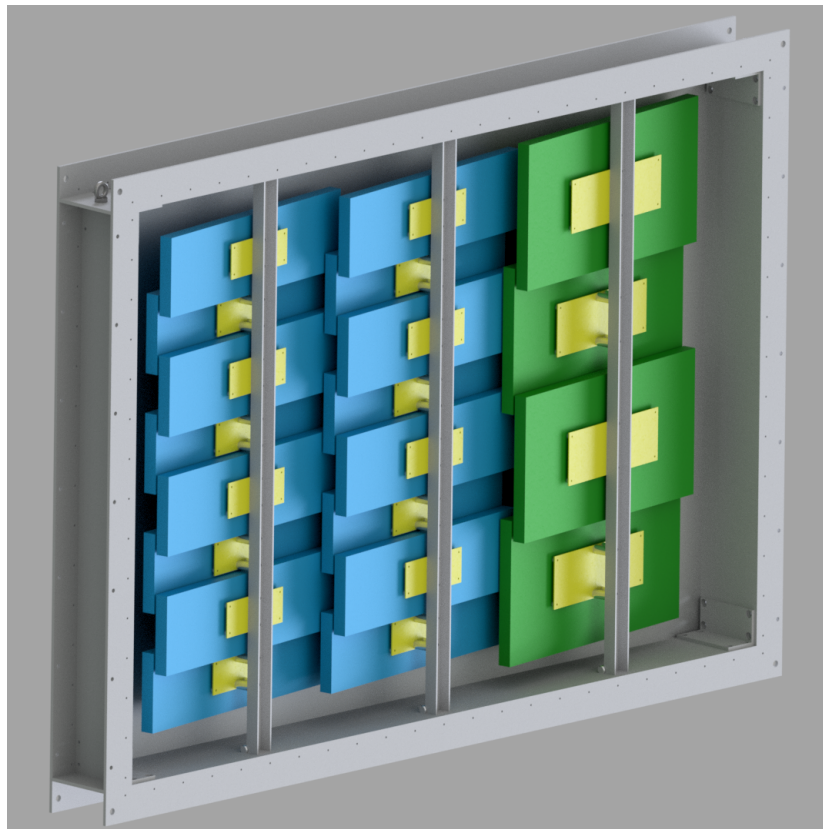


Figure 48: Design of the TOF-L module with mounted "wide" (green) and "narrow" (blue) MRPCs.

5.6.2 Tests

Three tests of a "wide" MRPC were performed: in December 2016 using a proton beam of 30AGeV/c, in August 2018 in the halo of the proton beam of 150AGeV/c and in November 2018 with an additional "wide" MRPC using the Pb beam of 150AGeV/c. During the tests two pad readout MRPCs were used as reference. Signals from the detectors were amplified by the NINO front-end electronics (FEE) [96] and by prototypes of analogue ampli-

fiers. An HPTDC-based TDC [97] was used as readout system for the NINO FEE. Signals from the analogue FEE were digitized by DRS4 modules. The main motivation of this measurement were the following: test the proper functioning of the MRPC, test of new analogue front-end electronics and synchronization of the HPTDC-based VME DAQ with the NA61/SHINE DAQ. The first results were described in the Addendum to the NA61/SHINE Proposal SPSC-P-330 [72]. Synchronization of DAQ as well as good time resolution of the MRPC with NINO electronics were achieved. Time resolution between the strip MRPC and pad MRPC was 75 ps and was stable during all tests. This result corresponds to a time resolution of ~ 50 ps for the strip MRPC (see Fig. 49). Meanwhile tests showed that analogue electronics can be used instead of NINO electronics for the precise time measurement. But more detailed R&D of the electronics is needed.

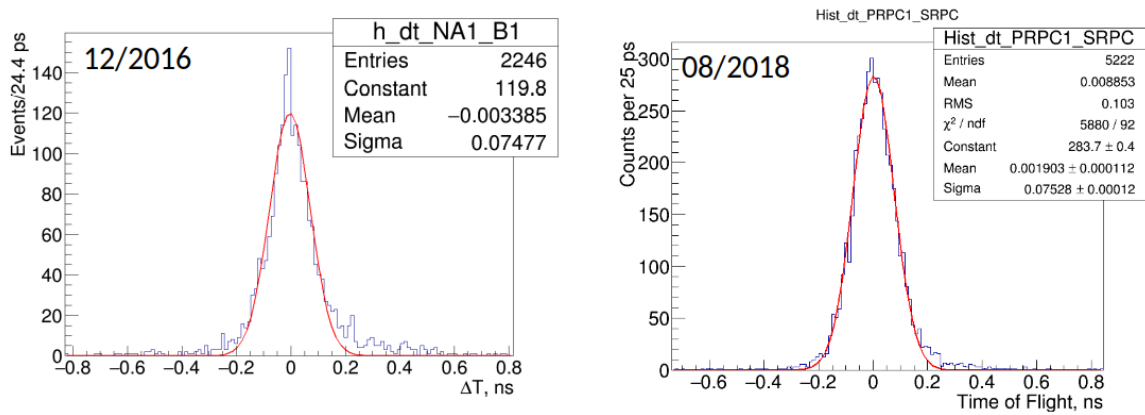


Figure 49: The time spectra of difference between the strip MRPC and MRPC with pad readout. *Left:* Spectra obtained in 2016. *Right:* Spectra obtained in 2018.

5.6.3 Gas system

The typical gas mixture used in the new MRPC system will consists of 90% Freon R134a, 5% iso-butane and 5% SF₆. The main component is C₂H₂F₄ (R134a). Its content in the mixture will always be at least 80%. The other two components may vary from 0% to 20%. The gas mixture must be supplied to each box independently. Although the gas volume of the detector is relatively small, the high cost of the gas mixture makes a closed loop circulation system necessary. The design parameters of the system are shown in Table 4.

Investigations of the gas mixture of the MRPC for the ALICE TOF found that the use of the flammable gas isobutane was not necessary [98]. Using a gas mixture without iso-C₄H₁₀ required an increase of the operating voltage which did not lead to degradation of the detector performance. However, the use of iso-butane is kept as a backup option with the possibility of abandoning it in the future. Therefore suitable precautions should be taken to close down the mixer unit if the mixture approaches the lower flammable limits. Extensive tests are under way to check the performance of the detector without iso-C₄H₁₀ in the gas mixture.

Table 4: Design parameters of the TOF gas system.

Parameter	Value
Total volume	1 m ³
Number of modules	2
Gas mixture	C ₂ H ₂ F ₄ / i-C ₄ H ₁₀ / SF ₆ (90%/5%/5%)
Volume exchange/day	~ 7
Total flow rate	300nl/h
Fresh gas flow rate	3nl/h
Working pressure	< 3 – 5 mbar
Tolerable O ² content	1000 ppm
Tolerable H ² O content	100 ppm

5.7 Software Upgrade

Extensive software development is currently underway to meet the NA61/SHINE data-taking demands after Long Shutdown 2. The main points of development are:

- (i) Online reconstruction software
- (ii) Calibration software
- (iii) Offline reconstruction and analysis software

Online reconstruction is being implemented as a method of data compression in order to maintain the 1 kHz data rate. TPC clusterization, local tracking, and noise rejection will be performed as data is acquired.

Current data-taking methods are not maintainable beyond Long Shutdown 2. With the expected increase in event rate, the data recorded by TPCs alone in 2021 and 2022 would total over 12 petabytes (PB). The online reconstruction and noise rejection software being developed reduces the stored data size by over 80%.

The online reconstruction software, based on the SHINE-native Cellular Automaton reconstruction, will run directly on the Event Builder nodes of the Data Acquisition system (DAQ). These nodes first run a fast clusterization algorithm to compress the initial raw data. The resulting clusters are fed into the TPC local tracking package, which finds and constructs tracks within each chamber. Clusters not associated with local tracks are recognized as electronic noise artifacts and rejected. Fig. 50 shows an example event taken from the 2018 High-Intensity Pb+Pb interactions at 150A GeV/c beam momentum. The left panel shows the event with no noise rejection, while the right panel shows the event after noise rejection has been performed.

As the reconstruction software is being run in an online manner, speed performance is critical. 160 Event Builders are available for online event processing, resulting in a maximum allowed processing time per event of 5.7 seconds. Recent improvements in the local tracking algorithm have resulted in a reconstruction time of 3.1 seconds per event for the heaviest and most energetic systems NA61/SHINE will record.

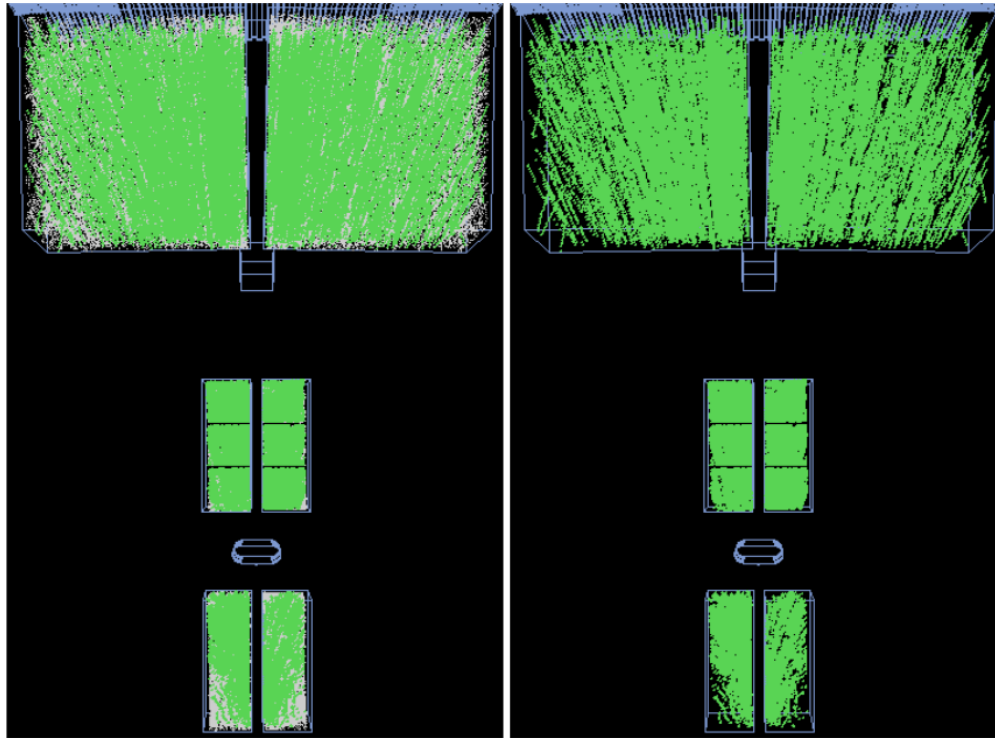


Figure 50: *SHINE* online reconstruction software and noise rejection. Left panel: Typical reconstructed Pb+Pb event at beam energy of 150 A GeV. Grey points indicate electronic noise, while green points correspond to clusters comprising local TPC tracks. Right panel: The same event processed with *SHINE*'s online noise filtering software.

Offline software, including calibration procedures, reconstruction modules, and analysis frameworks, are also seeing improvements and upgrades triggered by the inclusion of new detectors in NA61/SHINE. Significant development will continue in the following months.

5.8 Upgrade funding and spending profiles

In May 2019 NA61/SHINE submitted a Memorandum to the Director for Research and Computing Eckhard Elsen and the CERN Research Board. This memorandum presented an updated schedule of the NA61/SHINE detector upgrade which is conducted during the Long Shutdown 2. Due to uncertainties in the upgrade funding two scenarios were presented: the default scenario which leads to the first physics data taking in 2021 and the contingency scenario which leads to the first physics data taking in 2022.

Updated versions of default and contingency spending profiles are shown in Tables 5 and 6. Additionally the tables present the planned source of funding for both scenarios.

The contingency spending profile takes into account possible reductions of the cost: TPC low-voltage system based on industrial power supplies (reduction of 80k CHF), use of different connectors on the readout adapter boards (reduction of 20k CHF), use of an existing

Table 5: Default spending profile of the NA61/SHINE upgrade. Sources of funding are shown in the last column: already allocated in green, requests under submission or planned in the near future in black.

year	2018	2019	2020	2021	2022	sum	source of funding
TPC upgrade	-	115k	459k	-	-	574k	DFG grant (44%), CF (22%) or Polish/Norwegian Grant (66%), US DOE SHINE Request (17%), CF (17%)
VD	-	-	130k	-	-	130k	NCN OPUS (100%)
PSD	-	55k	-	-	-	55k	INR grant - contribution to NA61-CF (55%), NA62 payment for old PSD (45%)
MRPC ToF	50k	90k	376k	10	-	526k	JINR grant (100%)
BPD	-	-	60k	-	-	60k	NCN/DFG Beethoven (100%) or Japan grant (100%)
TDAQ	30k	93k	93k	-	-	216k	NCN Maestro (55%), NCN/DFG Beethoven (24%), CF 2018 (21%)
DRS4	-	40k	90k	-	-	130k	US DOE SHINE Request (55%), JINR grant (16%), CF (29%)

storage disk array (from Alice) in the TDAQ system (reduction of 52k CHF), re-use of a computer farm (from Alice) for the DRS4 readout nodes (reduction of 30k CHF), re-use of old VME crates with exchange of power supplies for the DRS4 readout system (reduction from 18 to 8k CHF).

Table 6: Contingency spending profile of the NA61/SHINE upgrade. Green color shows sources of funding are already allocated, black color funds to be covered from the NA61/SHINE-CF.

year	2018	2019	2020	2021	2022	sum	source of funding
TPC upgrade	-	115k	165k	175k	-	455k	CF (100%)
VD	-	-	-	40k	90k	130k	CF (100%)
PSD	-	55k	-	-	-	55k	INR grant - contribution to NA61-CF (55%), NA62 payment for old PSD (45%)
MRPC ToF	50k	90k	376k	10k	-	526k	JINR grant (100%)
BPD	-	-	30k	-	30k	60k	CF (100%)
TDAQ	30k	93k	41k	-	-	164k	NCN Maestro (73%), CF 2018 (27%)
DRS4	-	40k	20k	-	30k	90k	JINR grant (23%), CF (77%)

A summary of the financial resources requested from the NA61/SHINE-CF in the contingency spending profile is shown in Table 7. The average yearly income of the NA61/SHINE-CF is at the level of 210k CHF and should allow to follow the presented scenario.

Table 7: Spending profile from NA61/SHINE-CF in the contingency scenario.

year	2018	2019	2020	2021	2022	sum
Requested amount	30	155k	195k	215k	150k	745k

5.8.1 CERN resources

In order to prepare for the post LS2 operation of NA61/SHINE, modifications are necessary in the PPE142/152 zone. Modification of the zone(s) layout, as well as the involvement of several CERN groups and services is necessary for the detector upgrades. The costs and schedule of this work, as agreed with the relevant CERN groups, are described in detail in Ref. [99]. The total support requested by NA61/SHINE is at the level of 172k CHF and includes installation of the scaffolding, installation of a local chiller for LV TPC electronics, update of the electrical line and the raw water line, radiation shielding for the F-PSD area and IT resources needed during the first year of data taking.

6 Summary

This NA61/SHINE annual report briefly presents the status and plans of the NA61/SHINE experiment [1] at the CERN SPS. The report refers to the period October 2018 – October 2019.

The summary of this report is as follows:

(i) Recorded physics data (see Section 2):

- (a) Additional data on p+(NOvA replica target) interactions at 120 GeV/c were collected at the beginning of November 2018 within the programme of measurements for the Fermilab neutrino beams.
- (b) Data on Pb+Pb collisions at 150A GeV/c were recorded in November 2018 as scheduled. These data were requested for the strong interaction programme of NA61/SHINE.
- (c) Pilot data on (light ion)+p interactions at 13A GeV/c were recorded in December 2018. The data were requested within the NA61/SHINE cosmic-ray programme to study the feasibility of measuring nuclear fragmentation needed for cosmic-ray physics.

(ii) Software and calibration modifications (see Section 3), in particular, include:

- (a) The native SHINE reconstruction software is almost completed.
- (b) NA61/SHINE software infrastructure changes follow the CERN IT infrastructure development plan.
- (c) The data calibration and reconstruction is progressing well.

(iii) New physics results, final and preliminary, were released, see Section 4. They include results relevant for the NA61/SHINE study of the onsets of deconfinement and fireball and search for the critical point:

- (a) results on collision energy dependence of the K^+/π^+ ratio in Ar+Sc collisions show no "horn"-structure,
- (b) results on collision energy dependence of the K^+/π^+ ratio and inverse slope parameter of kaon transverse mass spectra in p+p interactions show that the break in the rate of increase in p+p is close to the energy of the Pb+Pb "horn".
- (c) rapidity dependence of anisotropic flow relative to the spectator plane in Pb+Pb collisions at 13A GeV/c changes qualitatively with collision centrality.
- (d) two-pion correlations in Be+Be collisions at 150A GeV/c show no effects which can be related to the critical point.

Further new physics results within the strong interaction programme concern:

- (a) $K^*(892)^0$ production in p+p interactions at 40 and 80 GeV/c,
- (b) Ξ^+ spectra and Ξ^+/Ξ^- ratios in p+p interactions at 158 GeV/c,
- (c) Pentaquark $\Xi(1860)^{--}$ search in p+p collisions at 158 GeV/c,
- (d) First signal of D mesons in Xe+La collisions at 150A GeV/c.

The results obtained within the NA61/SHINE reference measurements for long-baseline neutrino oscillation experiments at J-PARC and Fermilab as well as cosmic-ray experiments (CR-A, CR-G) include:

- (a) Final results on hadron emission from the T2K replica-target (J-PARC),
- (b) Production cross section of p+C interactions at 31 GeV/c (J-PARC),
- (c) Cross section of p+Be/C/Al interactions at 60 and 120 GeV/c (FNAL),
- (d) Hadron spectra in π^+ +Be/C interactions at 60 GeV/c (FNAL),
- (e) \bar{p} spectra in π^- +C interactions at 158 and 350 GeV/c (CR-A),
- (f) Cross section of $C+p \rightarrow B + X$ at 13A GeV/c (CR-G).

(iv) Detector upgrade progress and plans are reported in Section 5:

- (a) The upgrade of TPC read-out, Trigger and DAQ, PSD, DCS, MRPC is progressing according to schedule.
- (b) A decision whether the funding will allow for the first physics data taking in 2021 (the default scenario) or in 2022 (the contingency scenario) is planned to be made in February 2020

Acknowledgments

We would like to thank the CERN PH, BE and EN Departments for the strong support of NA61/SHINE.

This work was supported by the Hungarian Scientific Research Fund (grants OTKA 68506 and 71989), the János Bolyai Research Scholarship of the Hungarian Academy of Sciences, the Polish Ministry of Science and Higher Education (grants 667/N-CERN/2010/0, NN/202/48/4339 and NN/202/23/1837), the Polish National Center for Science (grants 2011/03/N/ST2/03691, 2012/04/M/ST2/00816, 2013/11/N/ST2/03879, 2014/14/E/ST2/00018, 2017/25/N/ST2/02575, and 2018/30/A/ST2/00226), the Foundation for Polish Science - MPD program, co-financed by the European Union within the European Regional Development Fund, the Ministry of Science and Education of the Russian Federation, grant No. 3.3380.2017/4.6, the National Research Nuclear University MEPhI in the framework of the Russian Academic Excellence Project (contract No. 02.a03.21.0005, 27.08.2013), the Federal Agency of Education of the Ministry of Education and Science of the Russian Federation (SPbSU research grant 11.38.193.2014), the Russian Academy of Science and the Russian Foundation for Basic Research (grants 08-02-00018, 09-02-00664 and 12-02-91503-CERN), the Ministry of Education, Culture, Sports, Science and Technology, Japan, Grant-in-Aid for Scientific Research (grants 18071005, 19034011, 19740162, 20740160 and 20039012), the German Research Foundation (grant GA 1480/2-2), the EU-funded Marie Curie Outgoing Fellowship, Grant PIOF-GA-2013-624803, the Bulgarian Nuclear Regulatory Agency and the Joint Institute for Nuclear Research, Dubna (bilateral contract No. 4418-1-15/17), Ministry of Education and Science of the Republic of Serbia (grant OI171002), Swiss Nationalfonds Foundation (grant 200020117913/1) and ETH Research Grant TH-01 07-3.

References

- [1] N. Antoniou *et al.*, [NA61/SHINE Collab.], “Study of hadron production in hadron nucleus and nucleus nucleus collisions at the CERN SPS,” 2006. CERN-SPSC-2006-034.
- [2] “European particle physics strategy update.” <https://europeanstrategyupdate.web.cern.ch/welcome>.
- [3] [NA61/SHINE Collab.], “Proposal from the na61/shine collaboration for the update of the european strategy for particle physics.” <https://indico.cern.ch/event/765096/contributions/3295521/>.
- [4] R. Alemany *et al.* [arXiv:1902.00260](https://arxiv.org/abs/1902.00260) [hep-ex].
- [5] A. Dainese *et al.*, [QCD Working Group Collab.] [arXiv:1901.04482](https://arxiv.org/abs/1901.04482) [hep-ex].
- [6] A. Dell’Acqua *et al.*, “Future Opportunities in Accelerator-based Neutrino Physics,” in *European Neutrino “Town” meeting and ESPP 2019 discussion Geneva, Switzerland, October 22-24, 2018*. 2018. [arXiv:1812.06739](https://arxiv.org/abs/1812.06739) [hep-ex]. <http://lss.fnal.gov/archive/2018/conf/fermilab-conf-18-688-nd.pdf>.
- [7] “Town meeting: Relativistic heavy ion physics.” <https://indico.cern.ch/event/746182/>.
- [8] S. Afanasev *et al.*, [NA49 Collab.] *Nucl.Instrum.Meth.* **A430** (1999) 210–244.
- [9] P. Podlaski, “Strangeness production at the CERN SPS energies,” 2019. https://indico.cern.ch/event/755366/contributions/3357938/attachments/1859695/3055901/SQM_Podlaski.pdf. Slides from 18th International Conference on Strangeness in Quark Matter (SQM 2019), Bari, Italy.
- [10] S. Pulawski, “Recent results from NA61/SHINE,” 2019. https://indico.cern.ch/event/755366/contributions/3427002/attachments/1859259/3055032/Pulawski_NA61_SQM2019.pdf. Slides from 18th International Conference on Strangeness in Quark Matter (SQM 2019), Bari, Italy.
- [11] M. Gazdzicki and M. I. Gorenstein *Acta Phys.Polon.* **B30** (1999) 2705, [arXiv:hep-ph/9803462](https://arxiv.org/abs/hep-ph/9803462) [hep-ph].
- [12] A. Aduszkiewicz *et al.*, [NA61/SHINE Collab.] *European Physical Journal* **C77** no. 10, (2017) 671, [arXiv:1705.02467](https://arxiv.org/abs/1705.02467) [nucl-ex].
- [13] E. Kashirin, O. Golosov, V. Klochkov, and I. Selyuzhenkov, “Anisotropic flow measurements from the NA61/SHINE and NA49 beam momentum scan programs at CERN SPS,” 2019. http://theor.jinr.ru/~wpcf2019/files/talks/07/8.%2020190607_WPCF_flow.pdf. Slides from XIV International Workshop Particle Correlations and Femtoscopy (WPCF2019), Dubna, Russia.
- [14] [NA61/SHINE Collab.]. <https://edms.cern.ch/document/1549298/1>.
- [15] [NA61/SHINE Collab.]. <https://edms.cern.ch/document/1867336/1>.
- [16] I. Selyuzhenkov and S. Voloshin *Phys. Rev.* **C77** (2008) 034904.
- [17] Y. Wu, [STAR Collab.] *Nucl. Phys.* **A982** (2019) 899–902, [arXiv:1807.06738](https://arxiv.org/abs/1807.06738) [nucl-ex].
- [18] V. Klochkov and I. Selyuzhenkov, [NA61/SHINE Collab.] *Nucl. Phys.* **A982** (2019) 439–442, [arXiv:1810.07579](https://arxiv.org/abs/1810.07579) [nucl-ex].
- [19] E. Kashirin, O. Golosov, V. Klochkov, and I. Selyuzhenkov, [NA49 Collab.] [arXiv:1810.07718](https://arxiv.org/abs/1810.07718) [nucl-ex].
- [20] B. Porfy, [NA61/SHINE Collab.], “NA61/SHINE results on Bose-Einstein correlations,” in *12th International Workshop on Critical Point and Onset of Deconfinement (CPOD 2018) Corfu, Greece, September 24-28, 2018*. 2019. [arXiv:1904.08169](https://arxiv.org/abs/1904.08169) [nucl-ex].
- [21] B. Porfy, [NA61/SHINE Collab.], “Levy HBT results at NA61/SHINE,” in *Proceedings, 18th Zimanyi School Winter Workshop on Heavy Ion Physics (Zimanyi School ’18): Budapest, Hungary, December 3-7, 2018*. 2019. [arXiv:1906.06065](https://arxiv.org/abs/1906.06065) [nucl-ex].
- [22] A. Adare *et al.*, [PHENIX Collab.] *Phys. Rev.* **C97** no. 6, (2018) 064911, [arXiv:1709.05649](https://arxiv.org/abs/1709.05649) [nucl-ex].
- [23] B. I. Abelev *et al.*, [STAR Collab.] *Phys. Rev.* **C80** (2009) 024905, [arXiv:0903.1296](https://arxiv.org/abs/0903.1296) [nucl-ex].
- [24] H. Beker *et al.* *Phys. Rev. Lett.* **74** (1995) 3340–3343.

- [25] C. Alt *et al.*, [NA49 Collab.] *Phys. Rev.* **C77** (2008) 064908, arXiv:0709.4507 [nucl-ex].
- [26] M. M. Aggarwal *et al.*, [STAR Collab.] *Phys. Rev.* **C83** (2011) 064905, arXiv:1004.0925 [nucl-ex].
- [27] A. Aduszkiewicz, [NA61/SHINE Collaboration Collab.], "Report from the NA61/SHINE experiment at the CERN SPS," Oct, 2018. <https://cds.cern.ch/record/2642286>.
- [28] N. G. Antoniou, F. K. Diakonos, A. S. Kapoyannis, and K. S. Kousouris *Phys. Rev. Lett.* **97** (2006) 032002, arXiv:hep-ph/0602051 [hep-ph].
- [29] N. Davis, "Searching for the critical point of strongly interacting matter in nucleus-nucleus collisions at CERN SPS," 2019. https://indico.cern.ch/event/577856/contributions/3424219/attachments/1879919/3097392/Davis_Intermittency_EPS_HEP2019.pdf. Slides from European Physical Society Conference on High Energy Physics (EPS-HEP2019), Ghent, Belgium.
- [30] S. V. Afanasiev *et al.*, [NA49 Collab.] *Phys. Lett.* **B491** (2000) 59–66.
- [31] A. Aduszkiewicz *et al.*, [NA61/SHINE Collab.] Submitted to *Eur. Phys. J. C* (2019) , arXiv:1908.04601 [nucl-ex].
- [32] A. Aduszkiewicz, [NA61/SHINE Collab.], "Report from the NA61/SHINE experiment at the CERN SPS," Tech. Rep. CERN-SPSC-2017-038. SPSC-SR-221, CERN, Geneva, Oct, 2017. <http://cds.cern.ch/record/2287091>.
- [33] A. Marcinek, [NA61/SHINE Collab.] *Nucl. Phys.* **A982** (2019) 855–858.
- [34] A. Tefelska, [CERN-NA-061 Collab.], " $K^*(892)^0$ production in p+p interactions at 158 GeV/c from NA61/SHINE," in *12th International Workshop on Critical Point and Onset of Deconfinement (CPOD 2018) Corfu, Greece, September 24-28, 2018*. 2019. arXiv:1905.09199 [nucl-ex].
- [35] K. Grebieszko, [NA61/SHINE Collab.], "New results on spectra and fluctuations from NA61/SHINE," in *12th International Workshop on Critical Point and Onset of Deconfinement (CPOD 2018) Corfu, Greece, September 24-28, 2018*. 2019. arXiv:1904.03165 [nucl-ex].
- [36] A. Tefelska, " $K^*(892)^0$ production in p+p interactions from NA61/SHINE," 2019. https://indico.cern.ch/event/755366/contributions/3357936/attachments/1861282/3059077/SQM_ATefelska_2019.pdf. Slides from 18th International Conference on Strangeness in Quark Matter (SQM 2019), Bari, Italy.
- [37] T. Anticic *et al.*, [NA49 Collab.] *Phys. Rev.* **C84** (2011) 064909, arXiv:1105.3109 [nucl-ex].
- [38] V. V. Begun, V. Vovchenko, M. I. Gorenstein, and H. Stoecker *Phys. Rev.* **C98** no. 5, (2018) 054909, arXiv:1805.01901 [nucl-th].
- [39] V. V. Begun, "private communication."
- [40] C. Alt *et al.*, [NA49 Collab.] *Phys. Rev. Lett.* **92** (2004) 042003, arXiv:hep-ex/0310014 [hep-ex].
- [41] Y. Ali *et al.* *Acta Phys. Polon.* **B44** (2013) .
- [42] N. Abgrall *et al.*, [NA61/SHINE Collab.] *Eur. Phys. J.* **C79** no. 2, (2019) 100, arXiv:1808.04927 [hep-ex].
- [43] N. Abgrall *et al.*, [NA61/SHINE Collab.] *Eur. Phys. J.* **C76** no. 11, (2016) 617, arXiv:1603.06774 [hep-ex].
- [44] L. Zambelli, A. Fiorentini, and T. Vladisavljevic, [T2K, NA61/SHINE Collab.] *J. Phys. Conf. Ser.* **888** no. 1, (2017) 012067.
- [45] L. Berns *et al.*, [T2K Beam group Collab.] "Developments of the flux MC tuning and consistency checks towards a reduction of the T2K neutrino beam flux", talk at the JPS meeting, September 2019, Japan .
- [46] A. Aduszkiewicz *et al.*, [NA61/SHINE Collab.] Submitted to *Phys. Rev. D* (2019) , arXiv:1909.03351 [hep-ex].
- [47] A. Carroll *et al.* *Phys. Lett.* **B80** (1979) 319.
- [48] S. Denisov *et al.* *Nucl. Phys.* **B61** (1973) 62.
- [49] S. R. Johnson, 2019. Ph.D. Thesis, University of Colorado Boulder.

- [50] A. Aduszkiewicz *et al.*, [NA61/SHINE Collab.] *Submitted to Phys. Rev. D* (2019) , arXiv:1909.06294 [hep-ex].
- [51] H.-J. Drescher and G. Farrar *Astropart. Phys.* **19** (2003) 235.
- [52] C. Meurer *et al.* *Czech. J. Phys.* **56** (2006) A211, arXiv:astro-ph/0512536 [astro-ph].
- [53] I. Maris *et al.* *Nucl. Phys. Proc. Suppl.* **196** (2009) 86, arXiv:0907.0409 [astro-ph.CO].
- [54] M. Unger, [NA61/SHINE Collab.] *Proc 32nd ICRC* **5** (2011) 67.
- [55] H. Dembinski, [NA61/SHINE Collab.] *Proc. 33rd ICRC* (2013) 688.
- [56] A. Herve, [NA61/SHINE Collab.] *PoS ICRC2015* (2016) 330, arXiv:1509.06586 [nucl-ex].
- [57] A. Aduszkiewicz *et al.*, [NA61/SHINE Collab.] *Eur. Phys. J.* **C77** (2017) 626, arXiv:1705.08206 [nucl-ex].
- [58] R. R. Prado, [NA61/SHINE Collab.] *PoS ICRC2017* (2018) 315, arXiv:1707.07902 [hep-ex].
- [59] R. R. Prado, [NA61/SHINE Collab.] *EPJ Web Conf.* **208** (2019) 05006, arXiv:1810.00642 [hep-ex].
- [60] N. Abgrall *et al.*, [NA61/SHINE Collab.] *Eur. Phys. J.* **C76** no. 2, (2016) 84, arXiv:1510.02703 [hep-ex].
- [61] Y. Genolini *et al.* *A&A* **580** (2015) A9.
- [62] N. Tomassetti *Phys. Rev.* **D96** (2017) 103005.
- [63] A. Reinert and M. W. Winkler *JCAP* **1801** (2018) 055.
- [64] C. Evoli, R. Aloisio, and P. Blasi *Phys. Rev.* **D99** no. 10, (2019) 103023, arXiv:1904.10220 [astro-ph.HE].
- [65] A. Aduszkiewicz *et al.*, [NA61/SHINE Collab.], "Feasibility Study for the Measurement of Nuclear Fragmentation Cross Sections with NA61/SHINE at the CERN SPS," 2017. CERN-SPSC-2017-035 ; SPSC-P-330-ADD-9.
- [66] H. Ströbele and I. Efthymiopoulos. *CERN Cour.*52N4 (2012) 33.
- [67] F. Sutter. "Messung der Fragmentation von Kohlenstoff auf Protonen zu Bor bei einer Energie von 13.5 A GeV", Master Thesis, Karlsruhe Institute of Technology, 2019.
- [68] M. Unger, [NA61/SHINE Collab.] *PoS ICRC2019* (2019) 446, arXiv:1909.07136 [astro-ph.HE].
- [69] M. Aguilar *et al.*, [AMS Collab.] *Phys. Rev. Lett.* **117** no. 23, (2016) 231102.
- [70] P. Fontes *Phys. Rev.* **C15** (1977) 2159.
- [71] Y. Genolini, D. Maurin, I. Moskalenko, and M. Unger *submitted to PRC* (2018) , arXiv:1803.04686 [astro-ph.HE].
- [72] A. Aduszkiewicz, [NA61/SHINE Collaboration Collab.], "Study of Hadron-Nucleus and Nucleus-Nucleus Collisions at the CERN SPS: Early Post-LS2 Measurements and Future Plans," Tech. Rep. CERN-SPSC-2018-008. SPSC-P-330-ADD-10, CERN, Geneva, Mar, 2018. <https://cds.cern.ch/record/2309890>.
- [73] K. Freese *EAS Publications Series* **36** (2009) 113–126, arXiv:0812.4005 [astro-ph].
- [74] F. Donato, N. Fornengo, and P. Salati *Physical Review D* **62** (2000) 043003, arXiv:hep-ph/9904481 [hep-ph].
- [75] N. Fornengo, L. Maccione, and A. Vittino *Journal of Cosmology and Astroparticle Physics* **1309** (2013) 031, arXiv:1306.4171 [hep-ph].
- [76] H. Baer and S. Profumo *Journal of Cosmology and Astroparticle Physics* **0512** (2005) 008, arXiv:astro-ph/0510722 [astro-ph].
- [77] F. Donato, N. Fornengo, and D. Maurin *Physical Review D* **78** (2008) 043506, arXiv:0803.2640 [hep-ph].

- [78] R. Duperray, B. Baret, D. Maurin, G. Boudoul, A. Barrau, L. Derome, K. Protasov, and M. Buénerd *Physical Review D* **71** no. 8, (Apr., 2005) 083013, [astro-ph/0503544](#).
- [79] A. Ibarra and S. Wild *Journal of Cosmology and Astroparticle Physics* **1302** (2013) 021, [arXiv:1209.5539 \[hep-ph\]](#).
- [80] L. Dal and A. Raklev *Physical Review D* **89** (2014) 103504, [arXiv:1402.6259 \[hep-ph\]](#).
- [81] A. Ibarra and S. Wild *Physical Review D* **88** (2013) 023014, [arXiv:1301.3820 \[astro-ph.HE\]](#).
- [82] A. Schwarzschild and Č. Zupanič *Physical Review* **129** (Jan, 1963) 854–862.
- [83] D. G. Coral, A. M. Rocha, V. Grabski, A. Datta, P. von Doetinchem, and A. Shukla *Phys. Rev. D* **98**, 023012 (2018), [arXiv:1806.09303](#) (2018) .
- [84] M. Korsmeier, F. Donato, and M. D. Mauro *Physical Review D* (2018) .
- [85] F. Becattini and U. W. Heinz *Zeitschrift für Physik C Particles and Fields C* **76** (1997) 269–286, [arXiv:hep-ph/9702274 \[hep-ph\]](#). [Erratum: *Z. Phys.*C76,578(1997)].
- [86] A. Andronic, P. Braun-Munzinger, J. Stachel, and H. Stöcker *Physics Letters B* **697** no. 3, (2011) 203 – 207.
- [87] J. Cleymans, S. Kabana, I. Kraus, H. Oeschler, K. Redlich, and N. Sharma *Physical Review C* **84** no. 5, (Nov., 2011) 054916, [arXiv:1105.3719 \[hep-ph\]](#).
- [88] M. Floris *Nuclear Physics A* **931** no. 0, (2014) 103 – 112.
- [89] A. Aduszkiewicz, [NA61/SHINE Collaboration Collab.], “Beam momentum scan with Pb+Pb collisions,” Tech. Rep. CERN-SPSC-2015-038. SPSC-P-330-ADD-8, CERN, Geneva, Oct, 2015. <https://cds.cern.ch/record/2059811>.
- [90] G. Aglieri Rinella, [ALICE Collab.] *Nucl. Instrum. Meth.* **A845** (2017) 583.
- [91] <https://opcfoundation.org/about/opc-technologies/opc-ua/>.
- [92] <https://open62541.org/>.
- [93] S. V. Afanasev, A. Isupov, V. I. Kolesnikov, A. I. Malakhov, G. L. Melkumov, and A. Yu. Semenov *JINR rapid communications* **5[85]-97** (1997) 69–90. [http://www1.jinr.ru/Archive/Pepan_letters/pan1_1997/5\[85\]-97_7.pdf](http://www1.jinr.ru/Archive/Pepan_letters/pan1_1997/5[85]-97_7.pdf).
- [94] V. A. Babkin *et al.* *JINST* **11** no. 06, (2016) C06007, [arXiv:1606.02286 \[physics.ins-det\]](#).
- [95] V. Babkin *et al.* *Nucl. Instrum. Meth.* **A824** (2016) 490–492.
- [96] M. G. Buryakov, V. A. Babkin, V. M. Golovatyuk, S. V. Volgin, and M. M. Romyantsev *Phys. Part. Nucl. Lett.* **13** no. 5, (2016) 532–534.
- [97] <http://afi.jinr.ru/TDC72VHL>.
- [98] A. N. Akindinov *et al.* *Nucl. Instrum. Meth.* **A532** (2004) 562–565.
- [99] S. Kowalski *et al.*, 2019. Modifications in PPE142/52 Zones for NA61 operation after LS2., <https://edms.cern.ch/ui/file/2093072/0.1>.